Akhavan-Tafti Mojtaba (Orcid ID: 0000-0003-3721-2114)
Slavin James, A. (Orcid ID: 0000-0002-9206-724X)
Le Guan (Orcid ID: 0000-0002-9504-5214)
Eastwood Jonathan, P. (Orcid ID: 0000-0003-4733-8319)
Strangeway Robert, J. (Orcid ID: 0000-0001-9839-1828)
Russell Christopher T. (Orcid ID: 0000-0003-1639-8298)
Nakamura Rumi (Orcid ID: 0000-0002-2620-9211)
Baumjohann Wolfgang (Orcid ID: 0000-0001-6271-0110)
Torbert Roy, B. (Orcid ID: 0000-0001-7188-8690)
Giles Barbara, L. (Orcid ID: 0000-0001-8054-825X)
Gershman Daniel, J (Orcid ID: 0000-0003-1304-4769)
Burch James, L (Orcid ID: 0000-0003-0452-8403)

MMS Examination of FTEs at the Earth's Subsolar Magnetopause

M. Akhavan-Tafti[1], J. A. Slavin[1], G. Le[2], J. P. Eastwood[3], R. J. Strangeway[4], C. T. Russell[4], R. Nakamura[5], W. Baumjohann[5], R. B. Torbert[6,7], B. L. Giles[2], D. J. Gershman[2,8], and J. L. Burch[7]

[1]Climate and Space Sciences and Engineering, University of Michigan, Ann Arbor, MI, USA.

[2]NASA Goddard Space Flight Center, Greenbelt, MD, USA.

[3]Blackett Laboratory, Imperial College London, London, UK.

[4]Department of Earth, Planetary and Space Sciences, University of California, Los Angeles, California, USA.

[5]Space Research Institute, Austrian Academy of Sciences, Graz, Austria.

[6]Institute for the Study of Earth, Oceans and Space, University of New Hampshire, Durham, New Hampshire, USA.

[7]Southwest Research Institute, San Antonio, Texas, USA.

[8]Department of Astronomy, University of Maryland, College Park, Maryland, USA.

Corresponding author: Mojtaba Akhavan-Tafti (akhavant@umich.edu)

This is the author manuscript accepted for publication and has undergone full peer review but has not been through the copyediting, typesetting, pagination and proofreading process, which may lead to differences between this version and the Version of Record. Please cite this article as doi: 10.1002/2017JA024681

Key Points:

- Flux ropes observed at sub-solar magnetopause have a mean diameter of 1700 km which is 3 to 7 times smaller than high-latitude flux ropes
- Field-aligned current dominates perpendicular current in the central regions of all quasi-force free flux ropes
- Plasma density dropping inside flux ropes as the core magnetic field strengthens indicates temporal evolution upon flux rope formation

Abstract

Determining the magnetic field structure, electric currents, and plasma distributions within flux transfer event (FTE)-type flux ropes is critical to the understanding of their origin, evolution, and dynamics. Here, the Magnetospheric Multiscale (MMS) mission's high-resolution magnetic field and plasma measurements are used to identify FTEs in the vicinity of the subsolar magnetopause. The constant-α flux rope model is used to identify quasi-force free flux ropes and to infer the size, the core magnetic field strength, the magnetic flux content, and the spacecraft trajectories through these structures. Our statistical analysis determines a mean diameter of 1700 ± 400 km (~ 30 ± 9 d_i) and an average magnetic flux content of 100 ± 30 kWb for the quasi-force free FTEs at the Earth's subsolar magnetopause which are smaller than values reported by Cluster at high latitudes. These observed non-linear size and magnetic flux content distributions of FTEs appear consistent with the plasmoid instability theory which relies on the merging of neighboring, small-scale FTEs to generate larger structures. The ratio of the perpendicular to parallel components of current density, R_J, indicates that our FTEs are magnetically force-free, defined as $R_J < 1$, in their core regions ($< 0.6\ R_{flux\ rope}$). Plasma density is shown to be larger in smaller, newly-formed FTEs and dropping with increasing FTE size. It is also shown that parallel ion velocity dominates inside FTEs with largest plasma density. Field-aligned flow facilitates the evacuation of plasma inside newly-formed FTEs while their core magnetic field strengthens with increasing FTE size.

1 Introduction

Magnetic reconnection is the underlying physical process responsible for the release of energy stored in magnetospheric magnetic fields that powers plasma heating and acceleration (e.g., *Yamada et al.*, 2010; *Gonzalez and Parker*, 2016). Flux Transfer Events (FTEs) are transient signatures of magnetic reconnection. FTEs are twisted open flux tubes associated with the transfer of plasma from the magnetosheath into the magnetosphere. FTEs are identified by a bipolar signature in the component of magnetic field normal to the magnetopause together with a maximum in the axial component of magnetic field [*Russell and Elphic*, 1979; *Rijnbeek et al.*, 1984]. The *Berchem and Russell* [1984] statistical study of ISEE observations concluded that FTEs are formed at low latitudes and move to the flanks and to high latitudes and toward the flanks due to the anti-sunward magnetosheath flow and $\boldsymbol{J}\times\boldsymbol{B}$ magnetic tension forces [e.g., *Kawano and Russell*, 2005; *Omidi and Sibeck*, 2007].

According to the magnetohydrodynamic (MHD) model of magnetic reconnection, low reconnection rates are expected in highly elongated current sheets [*Parker*, 1957]. However, 2D kinetic simulations have argued that laminar Sweet-Parker layers such as the magnetopause become unstable to the formation of plasmoids with increasing Lundquist number, $S \propto V_A\ L_{SP}\ \eta^{-1}$, where $V_A \propto B\ \rho^{-1/2}$ is the Alfven speed, L_{sp} is the Sweet-Parker current sheet thickness, and η is the resistivity (*Daughton et al.*, 2009; *Huang and Bhattacharjee*, 2010, 2013).

Plasmoids or magnetic islands are two-dimensional realizations of three-dimensional flux ropes. Plasmoid instability leads to the formation of secondary plasmoids which serve to enhance the reconnection rate [*Manheimer and Lashmore-Davis*, 1984; *Biskamp*, 2000]. Various studies have assessed the characteristics and the factors on which plasmoid instability, secondary island formation, and 'fast' reconnection depend (e.g., *Vishniac*, 1995a; *Eastwood et al.*, 2007; *Bhattacharjee et al.*, 2009; *Cassak et al.*, 2009; *Cassak and Drake*, 2009, *Wang et al.*, 2010; *Moser and Bellan*, 2012; *Comisso et al.*, 2016).

The transition between the slow and fast reconnection regimes is predicted to take place at the ion inertial length, d_i, [*Simakov and Chacón*, 2008] where the thinning of the Sweet-Parker current layer (electron diffisuion region (EDR) in the context of kinetic simulations) becomes quickly unstable to plasmoid formation leading to larger variations in the reconnection rate [*Daughton et al.*, 2006; *Fujimoto*, 2006; *Karimabadi et al.*, 2007; *Phan et al.*, 2007; *Daughton et al.*, 2009; *Wang et al.*, 2016]. Theoretical kinetic models and resistive MHD simulations have been employed to investigate the dynamics and distribution of plasmoids (e.g., *Richard et al.*, 1989; *Huang and Bhattacharjee*, 2010, 2013).

Due to the development of tearing mode instability, multiple X-line reconnection, a series of current filaments, can occur. Tearing mode instability is a particular type of resistive instability arising from the decoupling of magnetic field lines from the fluid [*Furth et al.*, 1963]. Multiple X-line reconnection gives rise to the generation of multiple flux ropes which are termed flux transfer events at the magnetopause [*Lee and Fu*, 1985]. *Finn and Kaw* [1977] and *Pritchett and Wu* [1979] envisioned a configuration in which, due to finite resistivity, coalescence instability leads to a merging of multiple plasmoids into a single plasmoid via secondary reconnection [*Wang et al.*, 2016]. For the purposes of this study, the magnetic reconnection occurring between two merging flux ropes is called 'secondary reconnection' [*Wang et al.*, 2016]. *Fermo et al.* [2010] studied in 2D the role of coalescence in the growth of magnetic islands. Here, coalescence is the merger of two smaller magnetic islands through reconnection into a single larger island. *Fermo et al.* [2011] provided observational evidence, based on Cluster FTE observations, to support this model of magnetic island, or in 3D, flux rope growth.

Simulations and observations have indicated the existence of a more developed reconnection event in the outflow region of the primary X line [*Divin et al.*, 2007; *Sitnov et al.*, 2009]. Kinetic 2D simulations of coalescence show that after the collapse of an intermediate X-line, neighboring magnetic islands are pushed together and merge via reconnection to form larger ones [*Daughton et al.*, 2011]. This resulting magnetic island in turn expands by progressively cooling down from the outer layer inwards, until pressure gradient between the internal and external plasmas is stabilized resulting in a temporarily stable condition [*Cazzola et al.*, 2015]. This process is repeated and larger scale islands are formed. Similarly, at the dayside magnetopause, multiple FTEs are believed to form due to the reconnection process and evolve into larger structure over time [*Fu and Lee*, 1985]. Previous studies have determined the size distribution and flux content of FTEs (e.g., *Hasegawa et al.*, 2006, 2010; *Wang et al.*, 2005;

Fermo et al., 2011; *Eastwood et al.*, 2012, 2016; *Pu et al.*, 2013; *Wang et al.*, 2017). These results indicate that FTEs are one to few Earth radii in size and contain 1-10 MWb in magnetic flux. However, these measurements are mostly gathered at higher altitudes and away from the subsolar region.

This study employs the Lepping-Burlaga constant-α flux rope model to determine the radius of FTEs and the impact parameter (IP) of the individual MMS trajectories through the flux ropes observed at the Earth's subsolar region and evaluates the cogency of this model using the Magnetospheric Multiscale (MMS) mission's high spatial and temporal resolution plasma and fields measurements. Physical properties of FTEs are investigated and the role of coalescence in FTE growth is emphasized. Our results indicate that 1) small-scale FTEs are observed at the magnetopause more frequently than previously reported, 2) electric currents inside growing FTEs help reduce magnetic forces over time, and 3) plasma density and core magnetic field are inversely related inside evolving FTEs.

2 Experimental Approach

2.1 Instrumentation and Data

MMS was launched in 2015, and it consists of four identical satellites with unprecedented temporal and spatial resolutions [*Burch et al.*, 2016a]. MMS orbits at an inclination angle of 28˚ with geocentric apogee and perigee of 12 and 1.2 R_E, respectively. The first phase of the mission targeted the Earth's dayside magnetopause at low latitudes. For this phase, regions of interest with radial distances greater than 9 R_E were identified during which all instruments are operated at their fastest cadence, producing burst-mode data.

The four spacecraft were maintained at an average tetrahedron size of ~10 km (~ 6 electron inertial lengths based on a plasma density of 12 cm^{-3}). The fast plasma experiment (FPI) data were captured at 30 ms cadence for electrons and 150ms for ions [*Pollock et al.*, 2016]. FPI moments are constructed from all-sky electron and ion distributions. The fluxgate magnetometer (FGM) operates at 128 vectors per second [*Russell et al.*, 2014].

The subsolar region was targeted to investigate FTEs shortly after they are generated by reconnection [*Fuselier et al.*, 2016]. In this study, the subsolar region is defined as 12 ± 22.5' Local Time and $X_{GSM} > 8$ R_E. Figure 1 illustrates the spacecraft trajectories (grey lines) as well as burst-mode intervals (red lines) in the Geocentric Solar Magnetospheric (GSM) equatorial plane for this region. Model magnetopause minimum and maximum boundaries are also plotted for reference [*Shue et al.*, 1998]. Our study uses the measurements taken during 55 orbital passes (11/03/2015 — 12/28/2015) and a total of 279 burst-mode intervals. The average burst-mode interval was 2.25 min in duration.

2.2 Method

Flux ropes are identified with their bipolar signature in the normal component of the magnetic field, corresponding to a peak in the axial component of the magnetic field. In LMN coordinates, these components translate into B_L and B_M, respectively [*Russell and Elphic*, 1978]. The peak in B_M insures the presence of a strong axial magnetic field component which is the distinctive characteristic distinguishing helical flux ropes from other similar magnetic structures.

The transformation from the GSM coordinate system into the LMN coordinate system was achieved via applying minimum variance analysis (MVA) of the magnetic field [*Sonnerup and Cahill*, 1967; *Sonnerup and Scheible*, 1998; *Xiao et al.*, 2004; *Teh et al.*, 2017]. MVA was performed on 30s, 60s, 120s, and full intervals of burst-mode magnetic field time series data to identify FTEs. Figure 2 provides a sample MMS FTE observed by the four probes at 13:04:34 UTC on 16 October 2015 at (8.3, 7.1, -4.8) R_E in GSM. During this encounter, the enhancement in $|\mathbf{B}|$ correlated with bipolar perturbation of B_L (positive-then-negative). *Eastwood et al.* [2016] originally reported the observation of this ion-scale FTE several minutes before encountering an electron dissipation region [*Burch et al.*, 2016b].

The high time cadence of FGM together with small-scale tetrahedron and the very accurate and precise positioning knowledge of the MMS spacecraft enable multi-dimensional spatial gradient methods [*Harvey*, 1998]. Here, we investigate stress balance inside FTEs using the current density computed by curlometer technique [*Dunlop et al.*, 1990, 2002; *Slavin et al.*, 2003b]. Current density is also calculated directly using high quality FPI data according to the formula $\mathbf{J} = e\,(n_i\,\mathbf{v}_i - n_e\,\mathbf{v}_e)$ where n and v are the zeroth (number density) and first (bulk velocity) plasma moments, respectively. Figure 2c-e show the plasma moment profiles. For comparison, the linear barycenteric value of $\mathbf{J}_{FPI}$ is calculated with Taylor series expansion (first-order approximation) of current density with respect to a reference spacecraft α. The term barycenter refers to the center of mass of the tetrahedron:

$$\bar{\mathbf{B}} = \mathbf{B}_\alpha + [\nabla\mathbf{B}\cdot(\bar{\mathbf{r}} - \mathbf{r}_\alpha)] \qquad (1)$$

where α indicates the satellite's number (α = 1, …, 4) and $\nabla\mathbf{B}$ is the gradient of the magnetic field vector:

$$(\nabla B)_{ij} = \frac{1}{N^2}\left[\sum_{\alpha\neq\beta}\left(B_{\alpha i} - B_{\beta i}\right)\left(r_{\alpha k} - r_{\beta k}\right)\right] R^{-1}_{kj}\,. \qquad (2)$$

Here, *r* and N are the position vector and the number of spacecraft, respectively, and R^{-1}_{kj} is the inverse of the *volumetric tensor*:

$$R_{kj} = \frac{1}{N}\sum_{\alpha=1}^{N} r_{\alpha k}\, r_{\alpha j}\,. \qquad (3)$$

The current density profile, denoted as J_{FPI} in Figure 2f, is derived from a single-probe plasma

measurements (MMS2). The ratio of perpendicular to parallel components of current density helps analyze stress balance inside the FTE [*Zhao et al.*, 2016]:

$$R_J = |\mathbf{J}_\perp| / |\mathbf{J}_{//}|$$

where $J_{//} = |\mathbf{J} \cdot \mathbf{B}| / |\mathbf{B}| = J\, cos(\theta_{JB})$ and $J_\perp = \sqrt{|\mathbf{J}|^2 - (J_{//})^2} = |\mathbf{B} \times (\mathbf{J} \times \mathbf{B})| / |\mathbf{B}|^2$. In other words,

$$R_J \equiv arctan\,(\theta_{JB}). \qquad (4)$$

In Figure 2g, the blue and green lines are calculated using current densities that are computed from the curlometer technique and all four FPI measurements at the barycenter, respectively, while the red line only takes into account the FPI measurements from a single spacecraft. Small R_J along the cross section of this FTE indicates that the structure is magnetically force-free (i.e. $\mathbf{J} \times \mathbf{B} = 0$).

The force-free flux rope model [*Burlaga*, 1988; *Lepping et al.*, 1990; *Slavin et al*., 2003a] can be applied to gain quantitative information about the size and flux content of FTEs. The model assumes flux ropes to be i) cylindrically symmetric, and ii) force-free ($\mathbf{J} \times \mathbf{B} = 0$ and $\nabla \mathbf{P} = 0$ where P denotes thermal pressure). Thus, current density, **J**, is linearly proportional to magnetic field, **B**, and the force law has the following solutions [*Lundqvist*, 1950]:

$B_R = 0,$	Radial component of **B**
$B_A = J_0 (\alpha r') B_0 ,$	Axial component of **B**
$B_T = J_1 (\alpha r') B_0 H.$	Tangential component of **B**

where J_0 and J_1 are zeroth and first order Bessel functions, respectively, and B_0 is the magnitude of the core field along the axis of flux rope, H is the handedness, and r' describes the fractional radial distance from the center of the flux rope, equal to zero at the core and one at the edge. The core of the structure is where the magnetic field magnitude is most significant and the edge of the structure refers to the outer boundary of the flux rope where magnetic field magnitude drops to a minimum and the normal component of the magnetic field peaks. The value at which J_0 reaches zero is a constant α=2.4048.

Previous statistical studies of the size and flux content distribution of FTEs relied on an implicit assumption that the spacecraft passes through the center of the structure (e.g., *Fermo et al.*, 2011). Here, we employ the force-free model to infer the impact parameter (i.e. distance from the center of the structure at the closest approach), radius, peak core magnetic field magnitude, and flux content of FTEs. Appendix A lists the steps for computing the size and flux content of flux ropes. Figure 2i provides a schematic depiction of an arbitrary pass through a flux rope by MMS spacecraft. In this figure, Y_0 is the impact parameter and R_0 is the actual flux rope radius. For more detail, see Appendix A. Figure 2j shows the chi-square profile of observed magnetic field components with respect to a cylindrically-symmetric constant-α flux rope model for the *Eastwood et al.* [2016] event. The modeled characteristic radius for this FTE is the radius at which the global extremum of the chi-squared profile is located.

3 Results and Discussion

3.1 FTE size distribution:

During a 2-month dayside phase of MMS (11/03/2015—12/28/2015), when MMS sampled the subsolar magnetopause, 63 FTEs were identified using the visual criteria listed in the Methods section. All FTEs were required to be detected by all four spacecraft, but this was generally the case due to the small spacecraft separation. Using the force-free model described in Appendix A, the size and flux content of each FTE was determined.

Our approach takes into account the trajectory of the spacecraft with respect to the center of the FTE. Previous studies of FTEs have been limited by the uncertainty associated with assuming that the spacecraft goes straight through the center of the FTE along the surface of the magnetopause. That assumption is especially prone to error for large impact parameters (i.e. trajectories passing farther away from the center of the FTE). Here, we have constrained our selection criteria to only include FTEs with impact parameter smaller than 0.5 ($IP \leq 0.5$) and the Pearson's chi-squared test value below $\chi^2 \leq 0.1$. Figure 3 summarizes the distributions of IP and chi-square parameters for the 63 FTEs detected in the MMS burst-mode intervals. Of these events, eight had impact parameters larger than 0.5 and chi-squared fit values larger than 0.1, thus were eliminated from our study.

Figure 4a is a histogram of the size distribution of 1098 FTEs observed by Cluster mission between 2001 and 2003 where the assumption was that the Cluster spacecraft trajectories intersected the central axis (i.e., IP=0) [*Fermo et al.*, 2011; *Wang et al.*, 2005]. The black dashed curve is an exponential fit of nominal diameter of 5300 km. Figure 4b demonstrates the histogram of the normalized size distribution of MMS observations of the 55 FTEs that met all our criteria. As previously indicated, the FTE size is determined using the force-free model. The red curve corresponds to an exponential fit with the nominal diameter of 1700 ± 400 km and 30 ± 9 d_i, where d_i is the average ion inertial length inside each FTE. The black dashed curve represents the results from the Cluster observations. The MMS spacecraft observe small-scale

FTEs at the subsolar magnetopause more frequently than Cluster satellites at high latitudes. This results in a decaying exponential fit whose mean is at least three times smaller than previously reported. It is important to note that the IP = 0 assumption underestimates both the diameter and the strength of the magnetic field in the core. The green curve corresponds to MMS observations assuming IP = 0 for all crossings. As expected, this assumption results in a mean diameter that is artificially lower than the actual value.

The relative size distribution of the 55 FTEs at the subsolar region are depicted in Figure 5a. The circles illustrate the diameter and the spatial distribution of the events in the equatorial plane. The mean diameter is 1700 km which corresponds to ~30 ion inertial lengths. Ion-scale FTEs are observed at the subsolar region shortly after they are formed by reconnection. On the other hand, massive FTEs are observed farther away from the subsolar magnetopause. Figure 5b shows a histogram of the magnetic flux content of all FTEs. Flux content is calculated using the modeled values of core magnetic field and FTE radius (See Appendix A-viii). The exponential decay fit (red curve) has a mean of 100 ± 30 kWb. This average flux content is nearly 3 orders of magnitude smaller than previously reported.

The larger FTEs, on average, contain less plasma and are likely "older". In Figure 6a, plasma density, N, is averaged across the cross section of individual FTEs and plotted against diameter. The 55 events are grouped into (bin width (BW) = 500 km) bins and the error bars are graphical representations of the variability of averaged plasma data within each bin ($\sigma_{mean} \equiv \sigma/\sqrt{n}$; where n is the number of events in each bin). Large FTEs are observed away from the subsolar magnetopause and are the result of multiple X-line reconnection [e.g., MMS: *Hwang et al.*, 2016; THEMIS and Cluster: *Hasegawa et al.*, 2006, 2010; *Liu et al.*, 2008; *Eastwood et al.*, 2012; Double Star: *Trenchi et al.*, 2011].

The average plasma density drops with increasing core magnetic field strength inside FTEs. Figure 6b depicts averaged plasma density inside individual FTEs binned (BW = 1 nT) and plotted against modeled core magnetic field values (using the force-free flux rope model). The x-intercept of the linear fit in Figure 6b indicates that there is an upper threshold on the core magnetic field ($|B|_{core}$<120 nT) at the dayside magnetopause. Flux ropes rely on plasmas to carry electric current for their existence, hence, flux ropes cannot exist beyond the above threshold where plasma density drops to zero. The y-intercepts in Figures 6a-b determine that in the absence of flux ropes (i.e. $\lambda \to 0$ or $|B|_{core} \to 0$), plasma density rises to typical subsolar magnetopause plasma density (N~30-50 cm^{-3}; [*Escoubet et al.*, 1997]).

3.2 Magnetic force-balance inside FTEs:

Forces across a force-free structure must balance. The MMS high resolution FPI plasma measurements complement multi-spacecraft analysis techniques in assessing our force-free selection criteria. In particular, R_J, the ratio of perpendicular component of current density to the

parallel component is examined. In Figure 7a, the normalized probability distribution functions (PDF) of R_J computed at the barycenter from particle moments (<FPI>; green) and curlometer technique (CURL; blue) for all observed data points are plotted. Here, we assume structures with $R_J < 1$ to be force-free. This assumption is mathematically equivalent to $arctan(\theta_{JB}) < 1$ or $k\pi - \pi/4 < \theta_{JB} < k\pi + \pi/4$; where k is an integer [e.g., *Zhao et al.*, 2016]. Figure 7b shows the normalized cumulative distribution function (CDF) of R_J. The ratio is calculated using the current density components from the curlometer technique at the barycenter (CURL). FPI current density components are also used to calculate the ratio at the barycenter (<FPI>), at individual spacecraft (FPI 1 S/C), and via averaging the four-spacecraft FPI measurements (AVG). The four methods unanimously indicate that, in general, 60 percent of the cross section of FTEs is force-free. Our findings indicate that all FTEs are force-free near the core and non-force-free in the outer boundary (> 0.6 $R_{flux\ rope}$). The ratio, R_J, from the current density calculated via averaging the four-spacecraft FPI measurements (AVG), in Figures 7b, is in good agreement with ratios from both CURL and <FPI>.

Figure 8a shows the evolution of the Hall term (i.e., net magnetic force) as a function of FTE diameter. Averaged $|J \times B|$ is computed at the barycenter of individual FTEs and binned and plotted against FTE diameter. It indicates that FTEs become more magnetically force-free as they grow larger (i.e., age). In other words, small-scale FTEs must grow via adiabatic expansion or non-adiabatic mechanisms (i.e., coalescence) in order to re-arrange magnetic field lines and reach lower energy state. Figure 8b illustrates a first-order approximation of magnetic pressure gradient force across each FTE:

$$\nabla P_m \sim \frac{B_{core}^2 - B_{edge}^2}{2\mu_0 R_{FR}}$$

where B_{core} and B_{edge} are the (force-free) modeled core magnetic field and the FTE boundary magnetic field magnitude, respectively, and R_{FR} is the modeled FTE radius. The plotted values are grouped into 500 km bins. Hence, the exponential fit here indicates that magnetic pressure gradient drops with increasing FTE size. That is to say, the densely populated magnetic field lines inside ion-scale FTEs become uniformly distributed across the cross section of the FTE with time via strong (oppositely-directed) magnetic curvature force:

$$\mathbf{J} \times \mathbf{B} = -\nabla P_m + (\mathbf{B} \cdot \nabla)\mathbf{B} / \mu_0 .$$

Here, the second term on the right-hand side is the magnetic curvature force. Furthermore, we conclude that FTEs become magnetically force free (x-intercept in Figure 8a) beyond ~ 9000 km.

Previous studies have investigated the reliability of the curlometer technique in measuring current density in different plasma regimes [*Perri et al.*, 2017; *Graham et al.*, 2016; *Ergun et al.*, 2016]. In particular, *Graham et al.* [2016] concluded that, in the absence of sharp spatial gradients (i.e. sub-proton scale structures), the parallel component of current density for both CURL and AVG are largely congruent. Figure 9 shows a scatter plot of all data points for

parallel components of J_{CURL} and $J_{<FPI>}$ (indicated by grey +). The red line specifies the orthogonal linear regression fit and indicates that there is very good agreement (correlation coefficient ~ 0.95) between the curlometer technique current density and the current density derived from plasma moments at the barycenter. In theory, a purely force-free structure lacks any sharp spatial gradients, therefore $J_{\| \, CURL} = J_{\| \, <FPI>} = (1/N) \sum_i \{(\mathbf{J_{FPI}})_i \cdot \mathbf{B_i} / |\mathbf{B_i}|\}$, where i = 1, …, N. However, our observations show that curlometer $J_{\|}$ gives slightly larger values than those computed using FPI moments at the barycenter, especially at higher magnitudes. The small y-intercept, in Figure 9, casts out the existence of any significant sources of (systematic or random) error in computing current density using either techniques.

3.3 Case study

Figure 10 summarizes the physical quantities of three ion-scale FTE-type flux ropes. Table I lists the coordinate transformation (GSE to LMN) eigenvalues (λ) and eigenvectors for all events. FTE axes are all in the y-direction, consistent with *Owen et al.* [2008], indicating that FTEs move duskward (dawnward) due to J×B force exerted by magnetosheath flow. Knowledge of the impact parameter enables spatial characterization of physical properties of FTEs. Impact parameter varies between zero and one, where IP = 0 at the core of the structure and IP = 1 at the edges. As listed in Figure 11, *Events 1-3* are classified by impact parameter: low ($IP \leq 0.1$), medium ($0.1 < IP \leq 0.3$), and high ($0.3 < IP \leq 0.5$) impact parameters.

Event 1 was captured on November 16, 2015 at 02:56:31 UT. During this event, the four MMS spacecraft crossed the magnetopause into the magnetosheath with average separation of 12 km and the tetrahedron quality factor (TQF) ~0.7, which compares the structure to a regular tetrahedron [*Fusilier et al*., 2016]. The cross section of the structure was estimated to be 700 km, using the force-free model assuming an estimated local flow velocity v_i ~ 185 km/s. This scale length is equivalent to 10 ion inertial lengths ($d_i = c/\omega_{pi}$ ~ 70 km). The spacecraft crossed nearly through the core of the structure (IP = 0.06; $\chi^2 \sim 2\times10^{-3}$). The core magnetic field was found to be $|B|_{core}$ ~ 49 nT which corresponds to 9 kWb total magnetic flux content.

On November 15, 2015 at 03:24:35 UT (*Event 2*) an ion-scale FTE was observed in the Earth's subsolar region. This event was 700 km in diameter (v_i~180 km/s; IP=0.24; $\chi^2 \sim 9\times10^{-3}$). With a modeled core B strength of 56 nT, this FTE contained about 10 kWb magnetic flux.

All four satellites sampled the outer boundary of a medium-size FTE (*Event 3*) on December 07, 2015. Similar to *Events 1&2*, this structure was only 1.5 seconds in duration corresponding to 1500 km in diameter and magnetic flux content of 40 kWb (IP = 0.4; $\chi^2 \sim 2\times10^{-2}$). The FTE was driven by a strong anti-sunward magnetosheath flow (v_i~340 km/s).

Plasma density and plasma beta dip at the closest approach. *Panels c* in Figure 10 depict plasma density profiles across the cross section of the FTE. The drop is most significant (30%)

closest to the core of the structure (IP $\leq$ 0.1). Near the core of FTEs, strengthening magnetic field together with a dip in plasma density result in a drop in the plasma beta profile. This indicates that magnetic pressure plays a greater role in driving the evolution of the structure closer to the core (i.e. magnetic pressure gradient force) while thermal pressure is dominant at the edges of FTEs. Weaker plasma beta observed at the core of the FTE is linked to the out-of-plane guide magnetic field [*Karimabadi et al.,* 1999; *Liu et al.,* 2009] and is believed to inhibit the development of anisotropic velocity distributions and subsequent instabilities (i.e. Weibel instability [*Weibel,* 1959]) [*Schoeffler et al., 2011*].

Plasma beta (the ratio of the plasma pressure to the magnetic pressure) is suggested to play a role in determining the extent of plasma energization during flux rope formation [e.g., *Phan et al.,* 2010]. Magnetic reconnection is credited for spawning significant changes in the particle distribution function for $\beta < 0.1$ [*Li et al.,* 2017] and is shown to be less proficient in plasmas with relatively large β ($\beta < 0.1$) [*Hoshino et al.,* 2001; *Drake et al.,* 2006b, 2010; *Oka et al.,* 2010]). Simulations have also attributed flux rope's shape, core magnetic field strengths, and evolution to plasma beta [*Karimabadi et al.,* 1999; *Schoeffler et al., 2011*]. Plasma beta drops with both increasing FTE size and FTE core magnetic field. In Figure 12, the mean plasma beta values are computed per FTE and are binned and plotted against both FTE diameter and the modeled core magnetic field magnitude. Here, the plasma beta dropping with increasing FTE size is an order of magnitude faster than the drop with strengthening core magnetic field. This indicates that plasma pressure must be dropping with much faster rate than the rate with which magnetic pressure increases inside evolving FTEs. This is consistent with the hypothesis that FTEs grow force-free via driving out plasma while their core magnetic field strengthens [*Ma et al.,* 1994].

Ions inside densely populated FTEs are evacuated by a dominantly-parallel ion velocity while ions inside less populated FTEs remain 'trapped' (i.e. $V_{\parallel} < V_{\perp}$) due to increasing perpendicular ion velocity [*Schindler,* 1979; *Paschmann et al.,* 1982]. The red shaded area in Figure 13 indicates that the parallel ion velocity dominates inside FTEs with larger plasma densities [see *Zhang et al.,* 2010]. Inside FTEs with lower plasma density, ion velocity is prominently perpendicular to the local magnetic field configuration indicating that ions are trapped inside the flux rope [*Speiser and Williams,* 1982]. This is reminiscent of the betatron acceleration inside evolving magnetic flux ropes [e.g., *Retinò et al.,* 2008; *Fu et al.,* 2011, 2013]. In this view, the internal and external forces result in a net force that can accelerate particles via betatron acceleration perpendicular to the local magnetic field [*Zhao et al.,* 2017]. The population with smaller pitch angles accelerated parallel to the magnetic field upon 'opening' of the field lines have already been evacuated leaving particles with large pitch angles behind. Future study will further investigate the composition and pitch angle distribution of cold populations inside FTEs.

Current density is enhanced and is predominantly field-aligned in the core regions of FTEs. At low IP, current density reaches a peak at the closest approach at which point the parallel

component of current density dominates. However, farther away from the core, current density is, in general, small with comparable parallel and perpendicular components (with localized variabilities), as shown in Figure 10.3.f [*Farrugia et al.*, 2016]. Average current density across each FTE (BW = 500 km) is shown to be inversely proportional to FTE size. The decaying exponential fit in Figure 14a indicates that current density decreases with increasing FTE diameter while magnetic field strengthen has a direct relationship with FTE size (or age), as indicated in Figure 14b.

In summary, Figures 12-14 demonstrate that in order for the FTEs to reach their lowest energy states, the excess plasma must be evacuated along the magnetic field, which are signified by parallel flows and field-aligned current densities, while the core magnetic field strengthens [*Saunders et al.*, 1984; *Ma et al.*, 1994; *Zhang et al.*, 2010; *Chen et al.*, 2017]. From this perspective, the weakening magnetic pressure gradient and the strengthening core magnetic field imply that the magnetic pressure must increase with increasing FTE size while thermal pressure drops [*Farrugia et al.*, 1998]. FTEs are force-free in their core regions. As discussed above, 60% of the cross section of FTEs are force-free. While near the core of the structure magnetic forces cancel out one another, as shown in Figure 10.1.g, non-zero net forces at the edges of the FTE drive the evolution of the FTE and are responsible for the large R_J observed across *Event 3*.

4 Conclusions

In this study, we analyzed 55 quasi-force free FTEs observed during 2 months of MMS's Phase-A when the four spacecraft were at near the subsolar magnetopause. These events were identified on the basis of their bipolar B_L, strong core magnetic field signatures, and further screened using the Lepping-Burlaga constant-α flux rope model. The fitting of the MMS magnetic field measurements to this force-free model also allowed us to determine the impact parameter of the spacecraft trajectory relative to the central axis of the flux rope as well as the radius, core magnetic field intensity and magnetic flux content of the FTEs. Only FTEs with MMS impact parameters less than 50% of the radius of the structure were considered. The size and magnetic flux content distributions of the 55 FTEs satisfying this selection criteria fit decaying exponentials and indicate a nominal diameter of 1700 km (equivalent to ~30 ion inertial lengths) and a mean magnetic flux content of 100 kWb. This diameter is by a factor of 3 - 7 smaller than the value reported by *Fermo et al.*, [2011] and *Wang et al.* [2005] based upon three years of Cluster data collected at the high-latitude magnetopause and low latitude flanks. The observed non-linear distributions appear consistent with the plasmoid instability theory where coalescence plays a significant role in generating large-scale FTEs (e.g., *Shibata and Tanuma*, 2001; *Loureiro et al.*, 2007; *Samtaney et al.*, 2009; *Daughton et al.*, 2009; *Fermo et al.*, 2010; *Huang and Bhattacharjee*, 2010; *Uzdensky et al.*, 2010).

The difference in the nominal diameter of FTEs at the Earth's dayside magnetopause between MMS and Cluster observations is almost certainly due to their different orbits. Other

contributing factors include different dynamic pressures at the two regions (Cluster low-latitude flanks and high-latitude magnetopause and MMS subsolar magnetopause), solar activity cycle for the two studies (Cluster 2001-2003 and MMS 2015), and different sample sizes (Cluster 1098 events and MMS 55 events). Our observations indicate that the ion-scale FTEs observed by MMS in the subsolar region must form locally only a short time before they are detected. These small, newly-formed FTEs are then advected away from the subsolar region toward the flanks and high latitude regions by the anti-sunward magnetosheath flow. During this process FTEs are thought to grow and evolve into larger structures through the coalescence of smaller flux ropes into larger ones [*Fermo et al.*, 2011].

The Cluster's orbit had a perigee of 4 R_E and an apogee of 19.6 R_E with a 90° inclination angle. The plane of Cluster's orbit precesses clockwise looking down from the north, and during planned phases the spacecraft extends outside of the magnetopause during which FTEs can be observed. MMS was launched into a 28° inclination orbit with geocentric perigee and apogee of 1.2 R_E and 12 R_E, respectively. Cluster FTEs are observed at both the high-latitude magnetopause and low-latitude flanks for both southward and northward IMF while the FTEs reported in this study have been observed at the subsolar region where FTEs are believed to be originally formed [*Kawano and Russell*, 1997a; *Berchem and Russell*, 1984; *Daly et al.*, 1984; *Russell et al.*, 1984]. Hence, Cluster's polar orbit may have contributed to the observation of dominantly larger FTEs. Other missions surveying the magnetopause, such as THEMIS and Double Star, have reported the presence of large-scale FTEs (one to few Earth radii in diameter) farther away from the subsolar magnetopause. In addition, although Cluster is well-equipped to detect small-scale FTEs (sub-second duration) with its high time cadence magnetic field measurements, the spacecraft lacks the high time-resolution MMS/FPI measurements to confidently identify these structures.

Current density, J, is by definition parallel to the local magnetic field in a force-free flux rope. Electric current may be determined using the curlometer technique or directly from plasma ion and electron measurements. We found that, on average, 60% of the cross section of all FTEs are, to a first-order approximation, magnetically force-free. Furthermore, the two current density calculation techniques were juxtaposed to confirm the reliability of the curlometer technique at the subsolar region. It is shown that, in the presence of sharp temporal or spatial magnetic field gradients, the curlometer technique computes slightly larger electric current density than that derived from FPI measurements.

Our inference of an impact parameter for each FTE encounter enables the structure and the evolution of FTEs to be studied as a function of distance from the core. Three ion-scale FTE-type flux ropes with different impact parameters were investigated and the following conclusions are drawn:

i) Plasma density and plasma beta dip at the core of a quasi-force free FTE-type flux rope, inhibiting instabilities (i.e. sausage or kink-mode instabilities),

ii) The FTE core magnetic field strengthens as plasma is evacuated,

iii) FTEs are magnetically force-free at the core which is due to the predominately field-aligned current density,

iv) Current density peaks at the core of the structure. In addition, current density decreases with increasing FTE size.

It is also shown that plasma density and plasma beta drop with increasing FTE size and with increasing FTE core magnetic field strength. Electric current density also plummets with increasing structure size. These trends suggest that the factors affecting the force balance inside FTEs change as FTEs evolve. This includes changing the dimension and morphology of the field lines (expansion or contraction [*Drake et al*, 2006a]) as well as the escape of plasma on the field lines at the time of FTE formation. The variations in plasma moments and magnetic and thermal forces as a function of FTE size and impact parameter are the subjects of future work.

Force-free flux ropes represent the minimum energy state for helical magnetic fields and mark the end point of their evolution [*Priest*, 1990]. Weakening current density indicates that the structure is becoming more magnetically force-free as it ages ($J \times B \rightarrow 0$) while the decrease in plasma density with increasing FTE size corresponds to the vanishing of the thermal pressure gradient forces ($\nabla P \rightarrow 0$). A future study will investigate forces inside [*Zhao et al.*, 2016] and outside of FTEs [*Pritchett et al.*, 1979, 1992]. Lastly, previous studies have concluded that FTEs extend on one side up through the magnetosheath and connect to the solar wind while their other end reaches into the polar ionosphere [*Varsani et al.*, 2014; *Owen et al.*, 2008; *Fear et al.*, 2007, 2008, 2010]. Further work aims to study the evolution in the magnetic connectivity of FTEs as a function of size and impact parameter, using MMS's high time resolution charged particle moments.

Acknowledgement

The authors acknowledge the MMS team efforts to make data available to the community through the MMS Science Data Center website (https://lasp.colorado.edu/mms/sdc/public/). We also would like to thank the Space Physics Environment Data Analysis Software (SPEDAS) developers for providing the community with adequate tools to access and analyze data. Helpful conversations with GangKai Poh of University of Michigan, MI and James Drake of University of Maryland, MD are acknowledged. Research at the University of Michigan was funded by the MMS Project at Southwest Research Institute under their prime contract; MMS NASA contract NNG04EB99C. One author (JPE) was supported by the United Kingdom Science and Technology Facilities Council (STFC) under grant ST/N000692/1.

Appendix A.

The steps involved in determining the size and flux content of FTEs from the Lepping-Burlaga constant-α flux rope model:

i) To enable comparison of FTE observation with modeled values, observation magnetic field data is transformed from LMN to (radial-axial-tangential) RAT coordinate system:

$$B_{A\text{-}Obsrv} = {}^{B_M}\!/_{|B|},$$

$$B_{T\text{-}obsrv} = \sqrt{\left[{}^{B_L}\!/_{|\boldsymbol{B}|}\right]^2 + \left[{}^{B_N}\!/_{|\boldsymbol{B}|}\right]^2}.$$

ii) The *closest approach* (CA) is defined as the point across the structure where $B_{A\text{-}Obsrv}$ reaches the peak magnitude. At CA, the ratio:

$${}^{Y_0}\!/_{R_0} = {}^{B_{A\text{-}Obsrv}}\!/_{B_{T\text{-}Obsrv}}$$

is used to determine the *impact parameter*. The impact parameter is the fractional distance that the spacecraft has passed from the flux rope core at CA, where Y_0 is the distance from the flux rope center and R_0 is the radius of the flux rope, both of which are unknown at this point.

iii) The velocity of the FTE is that of total ion velocity as measured by FPI outside the structure ($V_0 \sim V_i$). The spacecraft are assumed stationary (i.e. $V_0 >> V_{S/C}$). The distance, X_0, between the edge of the flux rope and the CA is $X_0 = V_0 t_0$, where t_0 is the time it takes the spacecraft to traverse from the edge of the flux rope to the CA:

$$t_0 = {}^{1}\!/_{2}\, \Delta t_{peak\text{-}to\text{-}peak}.$$

Here, $\Delta t_{peak\text{-}to\text{-}peak}$ is the duration of the flux rope.

iv) Axial and tangential components of observed magnetic field data are incrementally stepped through in order to compute X_i. Increments are equivalent to the resolution of the magnetic field measurements (i.e. 128 vectors/s).

v) For increasing values of X_i (from 0 to X_0), the fractional radial distance, r', is calculated using the Pythagorean theorem normalized with the flux rope radius R_0:

$$R_0^2 = X_0^2 + Y_0^2$$

and,

$$r' = {R_i}/{R_0} = \sqrt{\left({Y_0}/{R_0}\right)^2 + \left({X_i}/{R_0}\right)^2}$$

where impact parameter and R_0 are constants. $B_{A\text{-}Model}$ and $B_{T\text{-}Model}$ are the modeled components of magnetic field:

$$B_{A\text{-}Model} = J_0(\alpha \sqrt{\left({Y_0}/{R_0}\right)^2 + \left({X_i}/{R_0}\right)^2})B_0$$

$$B_{T\text{-}Model} = J_1(\alpha \sqrt{\left({Y_0}/{R_0}\right)^2 + \left({X_i}/{R_0}\right)^2})B_0 H$$

assuming B_0 and H are equal to unity, for simplicity. The actual value of B_0 will be determined later.

vi) Chi-square statistical test (i.e. goodness of fit) is applied to compare observed and modeled values of B_A and B_T:

$$\chi^2 = {1}/{N} \sum_{i=1}^{N} [(B_{A\text{-}Model} - B_{A\text{-}Obsrv})^2 + (B_{T\text{-}Model} - B_{T\text{-}Obsrv})^2]$$

where N is the number of data points.

vii) The flux rope radius, R_i, resulting in the minimization of χ^2 represents the best fit for the force-free flux rope model (i.e. $R_i = R_0$ at $\min(\chi^2)$). At this point, impact parameter is used to determine the absolute value of Y_0. Similarly, the flux rope's core field strength, B_0, at CA is:

$$B_0 = B_M \left({B_{A\text{-}Obsrv}}/{B_{A\text{-}Model}}\right)$$

Figure 2j represents the chi-squared profile of the ion-scale FTE. The curve has a minimum at R_0 ~ 430 km.

viii) Determination of R_0 and B_0 enable estimating the flux transported across the dayside magnetopause by a given FTE [*Eastwood et al.*, 2012]:

$$\Phi = \left(\frac{2\pi\, B_0\, R_0^2}{\alpha}\right) J_1(\alpha)\ .$$

References

Berchem, J., and C. T. Russell (1984), Flux transfer events on the magnetopause: Spatial distribution and controlling factors, J. Geophys. Res., 89, 6689–6703.

Biskamp, D., Magnetic Reconnection in Plasmas (Cam- bridge University Press, 2000).

Bhattacharjee, A., Huang, Y.-M., Yang, H., Rogers, B. (2009), Fast reconnection in high-Lundquist-number plasmas due to the plasmoid Instability, Phys. Plasmas 16, 112102 doi: 10.1063/1.3264103

Burch, J. L., T. E. Moore, R. B. Torbert, and B. L. Giles (2016a), Magnetospheric multiscale overview and science objectives, Space Sci. Rev.,199(1), 5–21, doi:10.1007/s11214-015-0164-9.

Burch J. L., et al. (2016b), Electron-scale measurements of magnetic reconnection in space, Science, doi:10.1126/science.aaf2939.

Burlaga, L. F., Magnetic clouds and force-free field with constant alpha, J. Geophys. Res., 93, 7217, 1988.

Cassak, P. A., Shay, M. A., Drake, J. F. (2009), Scaling of Sweet–Parker reconnection with secondary islands, Physics of Plasmas 16, 120702; doi: 10.1063/1.3274462.

Cassak, P. A. and Drake, J. F. (2009), The Impact of Microscopic Magnetic Reconnection on Pre-Flare Energy Storage, Astrophys. J. Lett., doi: 10.1088/0004-637X/707/2/L158.

Cazzola E., Innocenti M. E., Markidis S. et al 2015 PhPl 22 092901.

Chen, Y., Toth, G., Cassak, P. A., Jia, X., Gombosi, T. I., Slavin, J., Markidis, S., Peng, I. (2017) Global three-dimensional simulation of Earth's dayside reconnection using a two-way coupled magnetohydrodynamics with embedded particle-in-cell model: initial results, J. Geophys. Res., arXiv:1704.03803.

Comisso, L., Lingam, M., Huang, Y.-M. and Bhattacharjee, A. (2016) General theory of the plasmoid instability, PhPl, 23, 100702.

Daly, P. W., Saunders, M. A., Rijnbeek, R. P., Schopke, N., and Russell, C. T. (1984) The Distribution of Reconnection Geometry in Flux Transfer Events Using Energetic Ion, Plasma, and Magnetic Data, J. Geophys. Res. 89, 3843.

Daughton, W., J. Scudder, and H. Karimabadi (2006), Fully kinetic simula-tions of undriven magnetic reconnection with open boundary conditions, Phys. Plasmas, 13(7), 072101.

Daughton, W., Roytershteyn, V., Albright, B. J., Karimabadi, H., Yin, L., Bowers, K. J. (2009), Transition from collisional to kinetic regimes in large-scale reconnection layers, Phys. Rev. Lett. 103, 065004. doi: 10.1103/PhysRevLett.103.065004.

Daughton, W., V. Roytershteyn, H. Karimabadi, L. Yin, B. J. Albright, S. Gary, and K. J. Bowers (2011), Secondary island formation in collisional and collisionless kinetic simulations of magnetic reconnection, in AIP Conference on Modern Challenges in Nonlinear Plasma Physics, vol. 1320, edited by D. Vassiliadis, p. 144, Am. Inst. of Phys., College Park, Md, doi:10.1063/1.3544319.

Divin, A. V., I. Sitnov, M. Swisdak, and J. F. Drake (2007), Reconnection nset in the magnetotail: Particle simulations with open boundary conditions, Geophys. Res. Lett., 34, L09109, doi:10.1029/2007GL029292.

Drake, J. F., Swisdak, M., Che, H., and Shay, M. A. (2006a), Electron acceleration from contracting magnetic islands during reconnection, Nature, 443, 553–556.

Drake J. F., Swisdak M., Schoeffler K. M., Rogers B. N., and Kobayashi S. (2006b), Formation of secondary islands during magnetic reconnection, Geophys. Res. Lett., 33, L13105, doi:10.1029/12006GL025957.

Drake, J. F., Opher, M., Swisdak, M., & Chamoun, J. N. (2010), Ap. J., 709, 963.

Dunlop, M. W., A. Balogh, D. J. Southwood, R. C. Elphic, K.-H. Glassmeier, and F. M. Neubauer (1990), Configurational sensitivity of multipoint magnetic field measurements, in Proceedings of the International Workshop on Space Plasma Physics Investigations by Cluster and Regatta, ESA SP–306, pp. 23–28, Eur. Space Agency, Paris.

Dunlop, M. W., Balogh, A., Glassmeier, K.-H., and Robert, P. (2002), Four-point cluster application of magnetic field analysis tools: The curlometer, J. Geophys. Res., 107(A11), 1384, doi:10.1029/2001JA0050088.

Eastwood, J. P., T.-D. Phan, F. S. Mozer, M. A. Shay, M. Fujimoto, A. Retinò, M. Hesse, A. Balogh, E. A. Lucek, and I. Dandouras (2007), Multi-point observations of the Hall electromagnetic field and secondary island formation during magnetic reconnection, J. Geophys. Res., 112, A06235, doi:10.1029/2006JA012158.

Eastwood, J. P., Phan, T. D., Fear, R. C., Sibeck, D. G., Angelopoulos, V., Øieroset, M., and Shay, M. A. (2012), Survival of flux transfer event (FTE) flux ropes far along the tail magnetopause, J. Geophys. Res., 117, A08222, doi:10.1029/2012JA017722.

Eastwood J. P., et al. (2016), Ion-scale secondary flux ropes generated by magnetopause reconnection as resolved by MMS, Geophys. Res. Lett., 43, 4716–4724, doi:10.1002/2016GL068747.

Ergun, R.E., et al., (2016), Magnetospheric multiscale satellites observations of parallel electric fields associated with magnetic reconnection. Phys. Rev. Lett. 116, 235102.

Escoubet, C. P., A. Pedersen, R. Schmidt, and P. A. Lindqvist (1997), Density in the magnetosphere inferred from ISEE 1 spacecraft potential, J. Geophys. Res., 102(A8), 17595–17609, doi:10.1029/97JA00290.

Farrugia C. J., Rijnbeek, R. P., Saunders, M.A., Southwood, D. J., Rodgers, D. J. (1988), A multi-instrument study of flux transfer event structure, J. Geophys. Res., Space Physics 93 (A12), 14465-14477.

Farrugia, C. J., et al. (2016), Magnetospheric Multiscale Mission observations and non-force free modeling of a flux transfer event immersed in a super-Alfvénic flow, Geophys. Res. Lett., 43, 6070–6077, doi:10.1002/2016GL068758.

Fear, R. C., Milan, S. E., Fazakerley, A. N., Owen, C. J., Asikainen, T., Taylor, M. G. G. T., Lucek, E. A., Rème, H., Dandouras, I., and Daly, P. W. (2007), Motion of flux transfer events: a test of the Cooling model, Ann. Geophys., 25, 1669-1690, doi:10.5194/angeo-25-1669-2007.

Fear, R. C., Milan, S. E., Fazakerley, A. N., Lucek, E. A., Cowley, S. W. H., and Dandouras, I. (2008), The azimuthal extent of three flux transfer events, Ann. Geophys., 26, 2353-2369, doi:10.5194/angeo-26-2353-2008.

Fear R.C., Milan S.E., Lucek E.A., Cowley S.W.H., Fazakerley A.N. (2010), Mixed Azimuthal Scales of Flux Transfer Events. In: Laakso H., Taylor M., Escoubet C. (eds) The Cluster Active Archive. Astrophysics and Space Science Proceedings. Springer, Dordrecht.

Fermo, R. L., Drake, J. F., Swisdak, M. (2010), A statistical model of magnetic islands in a current layer, R. Phys. Plasmas 17, 010702.

Fermo R. L., Drake J. F., Swisdak M., and Huang K.-J. (2011), Comparison of a statistical model for magnetic islands in large current layers with Hall MHD simulations and Cluster FTE observations, J. Geophys. Res., 116, A09226, doi:10.1029/2010JA016271.

Finn, J. M. and P. K. Kaw (1977), Coalescence instability of magnetic islands, Phys. Fluids, 20, 72.

Fu, Z. F., and L. C. Lee (1985), Simulation of multiple X-line reconnection at the dayside magnetopause, Geophys. Res. Lett., 12(5), 291–294, doi:10.1029/GL012i005p00291.

Fu, H. S., Y. V. Khotyaintsev, M. André, and A. Vaivads (2011), Fermi and betatron acceleration of suprathermal electrons behind dipolarization fronts, Geophys. Res. Lett., 38, L16104, doi:10.1029/2011GL048528.

Fu, H. S., et al. (2013), Energetic electron acceleration by unsteady magnetic reconnection, Nature Physics 9, 426–430, doi:10.1038/nphys2664.

Fujimoto, K. (2006), Time evolution of the electron diffusion region and the reconnection rate in fully kinetic and large system, Phys. Plasmas, 13(7),072904.

Furth, H.P., Killeen, J., & Rosenbluth, M.N. (1963), Phys. Fluids, 6, 459.

Fuselier, S. A. et al. (2016) Magnetospheric Multiscale science mission profile and operations. Space Sci. Rev. 199, 77–103.

Gonzalez and Parker (2016), Magnetic reconnection concepts and applications, Springer.

Graham, D. B., et al. (2016), Electron currents and heating in the ion diffusion region of asymmetric reconnection, Geophys. Res. Lett., 43, 4691–4700, doi:10.1002/2016GL068613.

Harvey, C. C. (1998), Spatial gradients and the volumetric tensor, in Analysis Methods for Multi-spacecraft Data, edited by G. Paschmann and P. W. Daly, pp. 307–322, ESA Publ. Div., Noordwijk, Netherlands.

Hasegawa, H., Sonnerup, B. U. Ö., Owen, C. J., Klecker, B., Paschmann, G., Balogh, A., and Rème, H. (2006), The structure of flux transfer events recovered from Cluster data, Ann. Geophys., 24, 603–618.

Hasegawa, H., et al. (2010), Evidence for a flux transfer event generated by multiple X-line reconnection at the magnetopause, Geophys. Res. Lett., 37, L16101, doi:10.1029/2010GL044219.

Hoshino, M., T. Mukai, T. Terasawa, and I. Shinohara (2001), Suprathermal electron acceleration in magnetic reconnection, J. Geophys. Res., 106(A11), 25979–25997, doi:10.1029/2001JA900052.

Huang, Y.-M., Bhattacharjee, A. (2010), On the Distribution of Plasmoids In High-Lundquist-Number Magnetic Reconnection, Phys. Rev. Lett. 109, 265002, doi: 10.1103/PhysRevLett.109.265002.

Huang, Y.-M., Bhattacharjee, A. (2013), Plasmoid instability in high-Lundquist-number magnetic reconnection, Physics of Plasmas 20, 055702, doi: 10.1063/1.4802941.

Huang, S. Y., M. Zhou, Z. G. Yuan, H. S. Fu, J. S. He, F. Sahraoui, N. Aunai, X. H. Deng, S. Fu, Y. Pang, et al. (2015), Kinetic simulations of secondary reconnection in the reconnection jet, J. Geophys. Res. Space Physics, 120, 6188–6198, doi:10.1002/2014JA020969.

Hwang, K.-J., et al. (2016), The substructure of a flux transfer event observed by the MMS spacecraft, Geophys. Res. Lett., 43, 9434–9443, doi:10.1002/2016GL070934.

Karimabadi, H., D. Krauss-Varban, N. Omidi, and H. X. Vu (1999), Magnetic structure of the reconnection layer and core field generation in plasmoids, J. Geophys. Res., 104(A6), 12,313–12,326.

Karimabadi, H., W. Daughton, and J. Scudder (2007), Multi-scale structure of the electron diffusion region, Geophys. Res. Lett., 34, L13104, doi:10.1029/2007GL030306.

Kawano, H., and C. T. Russell (1997a), Survey of flux transfer events observed with the ISEE 1 spacecraft: Dependence on the interplanetary magnetic field, J. Geophys. Res., 102, 11,307–11,313.

Kawano, H., and C. T. Russell (2005), Dual-satellite observations of the motions of flux transfer events: Statistical analysis with ISEE 1 and ISEE 2, J. Geophys. Res., 110, A07217, doi:10.1029/2004JA010821.

Lee, L. C., and Z. F. Fu (1985), A theory of magnetic flux transfer at the Earth's magnetopause, Geophys. Res. Lett., 12(2), 105–108.

Lepping, R. P., J. A. Jones, and L. F. Burlaga (1990) Magnetic field structure of interplanetary magnetic clouds at 1 AU, J. Geophys. Res., 95, 11,957.

Li, X., Guo, F., Li, H., Li, G. (2017) Particle Acceleration during Magnetic Reconnection in a Low-beta Plasma, The Astr. J., 843, 1.

Liu, J., V. Angelopoulos, D. Sibeck, T. Phan, Z. Y. Pu, J. McFadden, K. H. Glassmeier, and H. U. Auster (2008), THEMIS observations of the dayside traveling compression region and flows surrounding flux transfer events, Geophys. Res. Lett., 35, L17S07, doi:10.1029/2008GL033673.

Liu, C. X., Jin, S. P., Wei, F. S., Lu, Q. M. & Yang, H. A. (2009), Plasmoid-like structures in multiple X line Hall MHD reconnection. *J. Geophys. Res. Sp. Phys.* **114,** 1–16.

Loureiro, N. F., A. A. Schekochihin, and S. Cowley (2007), Instability of current sheets and formation of plasmoid chains, Phys. Plasmas, 14, 100703.

Lundquist, S. (1950) Magnetohydrostatic fields, Ark. Fys., 2, 361.

Ma, Z. W., Otto, A., Lee, L. C. (1994) Core magnetic field enhancement in single X line, multiple X line and patchy reconnection. J Geophys Res 99:6125–6136.

Manheimer, W.M., & Lashmore-Davis, C. (1984), MHD Instabilities in Simple Plasma Configuration, Naval Research Laboratory, Washington.

Moser, A. L. and Bellan, P. M. (2012), Magnetic reconnection from a multiscale instability cascade, Nature 482, 379.

Oka, M., Phan, T.-D., Krucker, S., Fujimoto, M., Shinohara., I. (2010) Electron acceleration by multi-island coalescence. The Astrophysical Journal 714:1, 915-926.

Omidi, N., and D. G. Sibeck (2007), Flux transfer events in the cusp, Geophys. Res. Lett., 34, L04106, doi:10.1029/2006GL028698.

Owen, C.J., A. Marchaudon, M.W. Dunlop, A.N. Fazakerley, J.-M. Bosqued, J.P. Dewhurst, R.C. Fear, S.A. Fuselier, A. Balogh and H. Rème, Cluster observations of "crater" flux transfer events at the dayside high-latitude magnetopause, J. Geophys. Res., 113, A07S04, doi:10.1029/2007JA012701, 2008.

Parker, E. N. (1957), J. Geophys. Res. 62, 509, doi:10.1029/JZ062i004p00509.

Paschmann, G., Haerendel, G., Papamastorakis, I., Sckopke, N., Bame, S. J., Gosling, J. T., and Russell, C. T. (1982), Plasma and magnetic field characteristics of magnetic flux transfer events, J. Geophys. Res., 87(A4), 2159–2168, doi:10.1029/JA087iA04p02159.

Perri, S., Valentini, F., Sorriso-Valvo, L., Reda, A., Malara, F. (2017), On the estimation of the current density in space plasmas: Multi- versus single-point techniques, Planet. Space Sci., 140 (1), pp. 6-10.

Phan, T. D., Drake, J. F., Shay, M. A., Mozer, F. S., Eastwood (2007), Evidence for an Elongated (>60 Ion Skin Depths) Electron Diffusion Region during Fast Magnetic Reconnection J. P., Phys. Rev. Lett. 99, 255002.

Phan, T. D., et al. (2010), The dependence of magnetic reconne ction on plasma B and magnetic shear: Evidence from solar wind observations, Astrophys. J. Lett., 719, L199, doi:10.1088/2041-8205/719/2/L199.

Pollock, C., Moore, T., Jacques, A. et al. (2016), Space Sci Rev, 199: 331. doi:10.1007/s11214-016-0245-4

Priest, E. R. (1990) The equilibrium of magnetic flux ropes, Geophys. Monogr., 58, 1–22.

Pritchett, P. L., and C. C. Wu (1979), Coalescence of magnetic islands, Phys. Fluids, 22, 2140–2146.

Pritchett, P. L. (1992) The coalescence instability in collisionless plasmas. Physics of Fluids B: Plasma Physics 4:10, 3371-3381.

Pu, Z. Y., J. Raeder, J. Zhong, Y. V. Bogdanova, M. Dunlop, C. J. Xiao, X. G. Wang, and A. Fazakerley (2013), Magnetic topologies of an in vivo FTE observed by Double Star/TC-1 at Earth's magnetopause, Geophys. Res. Lett., 40, 3502–3506, doi:10.1002/grl.50714.

Retinò, A., et al. (2008), Cluster observations of energetic electrons and electromagnetic fields within a reconnecting thin current sheet in the Earth's magnetotail, J. Geophys. Res., 113, A12215, doi:10.1029/2008JA013511.

Richard, R. L., Walker, R. J., Sydora, R. D., Ashour-Abdalla, M. (1989), The coalescence of magnetic flux ropes and reconnection in the magnetotail. *J. Geophys. Res.* **94,** 2471–2483.

Rijnbeek, R. P., Cowley, S. W. H., Southwood, D. J., and Russell, C. T. (1984), A survey of dayside flux transfer events observed by ISEE 1 and 2 magnetometers, J. Geophys. Res., 89, 786–800, doi:10.1029/JA089iA02p00786.

Russell, C.T. & Elphic, R.C. (1978), Initial ISEE magnetometer results: magnetopause observations, Space Sci. Rev., 22: 681. doi:10.1007/BF00212619.

Russell, C. T., and R. C. Elphic (1979), ISEE observations of flux transfer events at the dayside magnetopause, Geophys. Res. Lett., 6, 33.

Russell, C. T., Berchem, J., and Luhmann, J. G. (1984), On the Source Region of Flux Transfer Events, IGPP Publ., No. 2571.

Russell C. T., B. J. Anderson, W. Baumjohann, K. R. Bromund, D. Dearborn, D. Fischer, G. Le, H. K. Leinweber, D. Leneman, W. Magnes, J. D. Means, M. B. Moldwin, R. Nakamura, D. Pierce, F. Plaschke, K. M. Rowe, J. A. Slavin, R. J. Strangeway, R. Torbert, C. Hagen, I. Jernej, A. Valavanoglou, I. Richter (2014) The Magnetospheric Multiscale Magnetometers, Space Sci. Rev., DOI 10.1007/s11214-014-0057-3.

Samtaney, R., N. F. Loureiro, D. A. Uzdensky, A. A. Schekochihin, and S. C. Cowley (2009), Formation of plasmoid chains in magnetic recon- nection, Phys. Rev. Lett., 103, 105004.

Saunders, M. A., Russell, C. T. and Sckopke, N. (1984) A Dual-Satellite Study of the Spatial Properties Of FTEs, in Magnetic Reconnection in Space and Laboratory Plasmas (ed E. W. Hones), American Geophysical Union, Washington, D. C.. doi: 10.1029/GM030p0145.

Schindler, K. (1979) On the role of irregularities in plasma entry into the magnetosphere, J. Geophys. Res., 84, 7257.

Schoeffler, K. M., Drake, J. F. & Swisdak, M. (2011), The Effects of Plasma Beta and Anisotropy Instabilities on the Dynamics of Reconnecting Magnetic Fields in the Heliosheath. *Astrophys. J.* 743**,** 70.

Shibata, K., and S. Tanuma (2001), Plasmoid-induced-reconnection and fractal reconnection, Earth Planets Space, 53, 473–482.

Shue, J.-H., et al., (1998) Magnetopause location under extreme solar wind conditions, J. Geophys. Res., 103(A8), 17,691–17,700.

Simakov, A. N. and Chacón (2008), Quantitative, Comprehensive, Analytical Model for Magnetic Reconnection in Hall Magnetohydrodynamics, L. Phys. Rev. Lett. 101, 105003.

Sitnov, M. I., M. Swisdak, and A. V. Divin (2009), Dipolarization fronts as a signature of transient reconnection in the magnetotail, J. Geophys. Res., 114, A04202, doi:10.1029/2008JA013980.

Slavin, J. A., R. P. Lepping, J. Gjerloev, D. H. Fairfield, M. Hesse, C. J. Owen, M. B. Moldwin, T. Nagai, A. Ieda, and T. Mukai (2003a) Geotail observations of magnetic flux ropes in the plasma sheet, J. Geophys. Res., 108(A1), 1015, doi:10.1029/2002JA009557.

Slavin, J. A., et al. (2003b), Cluster electric current density measurements within a magnetic flux rope in the plasma sheet, Geophys. Res. Lett., 30, 1362, doi:10.1029/2002GL016411, 7.

Sonnerup, B. U., and L. J. Cahill Jr. (1967), Magnetopause structure and attitude from Explorer 12 observations, J. Geophys. Res., 72(1), 171–183, doi:10.1029/JZ072i001p00171.

Sonnerup, B. U. O., and M. Scheible (1998), Minimum and maximum variance analysis, in Analysis Methods for Multi-Spacecraft Data, edited by G. Paschmann and P. Daly, pp. 185–220, Eur. Space Agency, Noordwijk, Netherlands.

Speiser, T. W., and D. J. Williams (1982), Magnetopause modeling: Flux transfer events and magnetosheath quasi-trapped distributions, J. Geophys. Res., 87(A4), 2177–2186, doi:10.1029/JA087iA04p02177.

Teh, W.-L., R. E. Denton, B. U. Ö. Sonnerup, and C. Pollock (2017), MMS observations of oblique small-scale magnetopause flux ropes near the ion diffusion region during weak guide-field reconnection, Geophys. Res. Lett., 44, doi:10.1002/2017GL074291.

Trenchi, L., M. F. Marcucci, H. Rème, C. M. Carr, and J. B. Cao (2011), TC-1 observations of a flux rope: Generation by multiple X line reconnection, J. Geophys. Res., 116, A05202, doi:10.1029/2010JA015986.

Uzdensky, D. A., N. F. Loureiro, and A. A. Schekochihin (2010), Fast magnetic reconnection in the plasmoid-dominated regime, Phys. Rev. Lett., 105(23), 235002.

Varsani, A., Owen, C. J., Fazakerley, A. N., Forsyth, C., Walsh, A. P., André, M., Dandouras, I., and Carr, C. M. (2014), Cluster observations of the substructure of a flux transfer event: analysis of high-time-resolution particle data, Ann. Geophys., 32, 1093-1117, doi:10.5194/angeo-32-1093-2014.

Vishniac, E.T. (1995a), The Dynamics of Flux Tubes in a High- beta Plasma. I. A General Description, ApJ, 446, 724.

Wang, Y. L., et al. (2005), Initial results of high-latitude magnetopause and low-latitude flux transfer events from 3 years of Cluster observations, J. Geophys. Res., 110, A11221, doi:10.1029/2005JA011150.

Wang et al. (2010), Phys. Rev. Lett. 104, 175003.

Wang, R. et al. (2016) Coalescence of magnetic flux ropes in the ion diffusion region of magnetic reconnection. Nat. Phys. 12, 263–267.

Wang, R., Lu, Q., Nakamura, R., Baumjohann, W., Russell, C. T., Burch, J. L., …, Gershman, D. (2017). Interaction of magnetic flux ropes via magnetic reconnection observed at the magnetopause. Journal of Geophysical Research: Space Physics, 122, 10,436–10,447. https://doi.org/10.1002/2017JA024482.

Weibel, E. S. (1959), Spontaneously Growing Transverse Waves in a Plasma Due to an Anisotropic Velocity Distribution. Phys. Rev. Lett. 2, 83–84.

Xiao, C. J., Z. Y. Pu, Z. W. Ma, S. Y. Fu, Z. Y. Huang, and Q. G. Zong (2004), Inferring of flux rope orientation with the minimum variance analysis technique, J. Geophys. Res., 109, A11218, doi:10.1029/2004JA010594.

Yamada et al. (2010), Rev. Mod. Phys. 82, 603.

Zhang, H., et al. (2010), Evidence that crater flux transfer events are initial stages of typical flux transfer events, J. Geophys. Res., 115, A08229, doi:10.1029/2009JA015013.

Zhao, C., et al. (2016), Force balance at the magnetopause determined with MMS: Application to flux transfer events, Geophys. Res. Lett., 43, 11, 941–11,947, doi:10.1002/2016GL071568.

Zhao, Y., R. Wang, and A. Du (2016), Characteristics of field-aligned currents associated with magnetic flux ropes in the magnetotail: A statistical study, J. Geophys. Res. Space Physics, 121, 3264–3277, doi:10.1002/2015JA022144.

Zhao A., Wang Y., Chi Y. et al 2017 SoPh 292 58.

Figure Captions

Figure 1. MMS Regions of interest (12 ± 22.5' MLT and X>7 R_E) in GSM coordinates (equatorial plane); shown in red are the Burst-mode intervals where the FPI time resolution is 30 ms for electrons and 150 ms for ions and FGM sample rate is 128 vectors/s. The grey lines are the spacecraft trajectories during November 03, 2015 through December 28, 2015.

Figure 2. The Eastwood 2016 event. *a)* total magnetic field, *b)* Magnetic field components in the LMN coordinates, *c)* ion (red) and electron (black) number densities, *d)* ion velocity in LMN coordinates, *e)* electron velocity in LMN coordinates, *f)* current density components, *g)* R_J (curlometer technique: blue, one spacecraft FPI current density: red, FPI current density at the barycenter: green), *h)* plasma beta. *i)* a cross-sectional view of a flux rope. The dashed line represents the trajectory of the spacecraft through the flux rope. The Closest Approach is indicated by Y_0 and R_0 and X_0 are the flux rope radius and the distance from the closest approach to the edge of the flux rope, respectively. X_i and R_i increase incrementally as the spacecraft travels farther toward the edge of the flux rope. *j)* Chi-square profile of the second *Eastwood et al.* [2016] event. The estimated FTE radius is comparable to that previously reported (~ 550 km).

Figure 3. Distribution of the identified FTE data where green indicates the properties of the events included in this study: impact parameter (IP) smaller than 0.5 and chi-squared values lower than 0.1.

Figure 4. *a)* Distribution of the diameters of 1098 Cluster flux transfer events with an exponential tail fit with λ_0 = 5280 km to the tail of the distribution assuming IP = 0 for all crossings [*Fermo et al.*, 2011], and *b)* A distribution of the diameters of 55 flux transfer events with IP < 0.5 and χ^2 < 0.1. The solid red line is the exponential fit of λ_0 = 1670 km. The black dashed curve corresponds to the FTEs observed by Cluster, as shown in panel *a*. The green curve is the exponential fit for the 55 events while assuming IP = 0 for all crossings.

Figure 5. *a)* Positions and size distributions of 55 FTEs in the GSM XY-plane; *b)* The distribution of the magnetic flux content of 55 flux transfer events with IP < 0.5 and χ^2 < 0.1. The solid red line is the exponential fit of Φ_0 ~ 100 kWb.

Figure 6. *a)* Bin-averaged (bin-width: BW=500 km) exponential fit of the FTEs' averaged number density and size; *b)* Bin-averaged (bin-width: BW=1 nT) linear regression of the FTEs' averaged number density and modeled core magnetic field.

Figure 7. *a)* Probability Distribution Function (PDF) of R_J. Blue indicates values that are computed using the curlometer technique while green signifies FPI measurement of current density at the barycenter. *b)* Cumulative Distribution Function (CDF) of R_J from the curlometer technique (blue), FPI measurements at the barycenter (green), and single-spacecraft FPI measurements (grey). The red diamonds are the average values for the four FPI measurements.

Figure 8. Bin-averaged (bin-width: BW=500 km) *a)* orthogonal linear regression of the FTEs' averaged net magnetic force (JxB) and diameter; *b)* exponential fit of the FTEs' averaged magnetic pressure gradient and diameter.

Figure 9. Orthogonal linear regression of the parallel components of curlometer and barycenter FPI current densities of all 70 FTE data points. Black dotted-line indicates unity correlation coefficient.

Figure 10. The flux rope-like FTEs (*Event1-3*): *a)* Magnetic field magnitude, *b)* observed (solid lines) and modeled magnetic field components (dashed lines) in LMN coordinates, *c)* ion density, *d)* ion parallel and perpendicular velocity components, *e)*, electron parallel and perpendicular velocity components, *f)* single spacecraft FPI current density, *g)* R_J (curlometer: blue, single-spacecraft FPI: red, and barycenter FPI: green), *h)* plasma beta (all four satellites).

Figure 11. Example low, mid, and high impact parameter trajectories through the structure.

Figure 12. Bin-averaged exponential fit of the FTEs' averaged plasma beta and *a)* FTE size (BW=500km), and *b)* FTE modeled core magnetic field magnitude.

Figure 13. Bin-averaged (BW=5 cm^{-3}) linear regressions between the FTEs' averaged number density and parallel (red diamond) and perpendicular ion velocities. Parallel and perpendicular ion flows dominate in the shaded red and blue patches, respectively.

Figure 14. Bin-averaged (BW=500 km) *a)* exponential fit between the FTEs' averaged (single-spacecraft FPI) current density magnitude, and *b)* linear regression between the modeled core magnetic field magnitude and the FTE size.

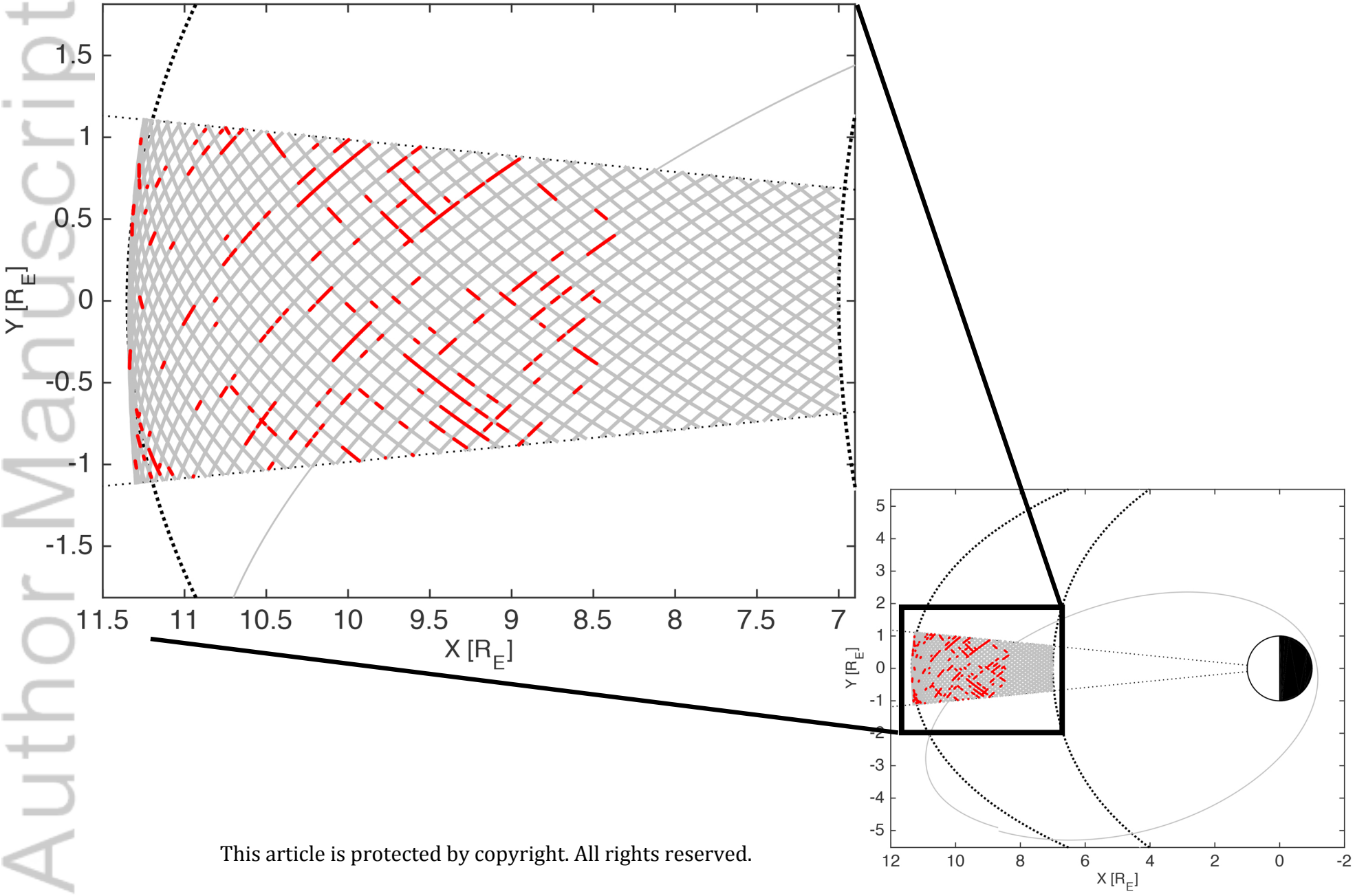

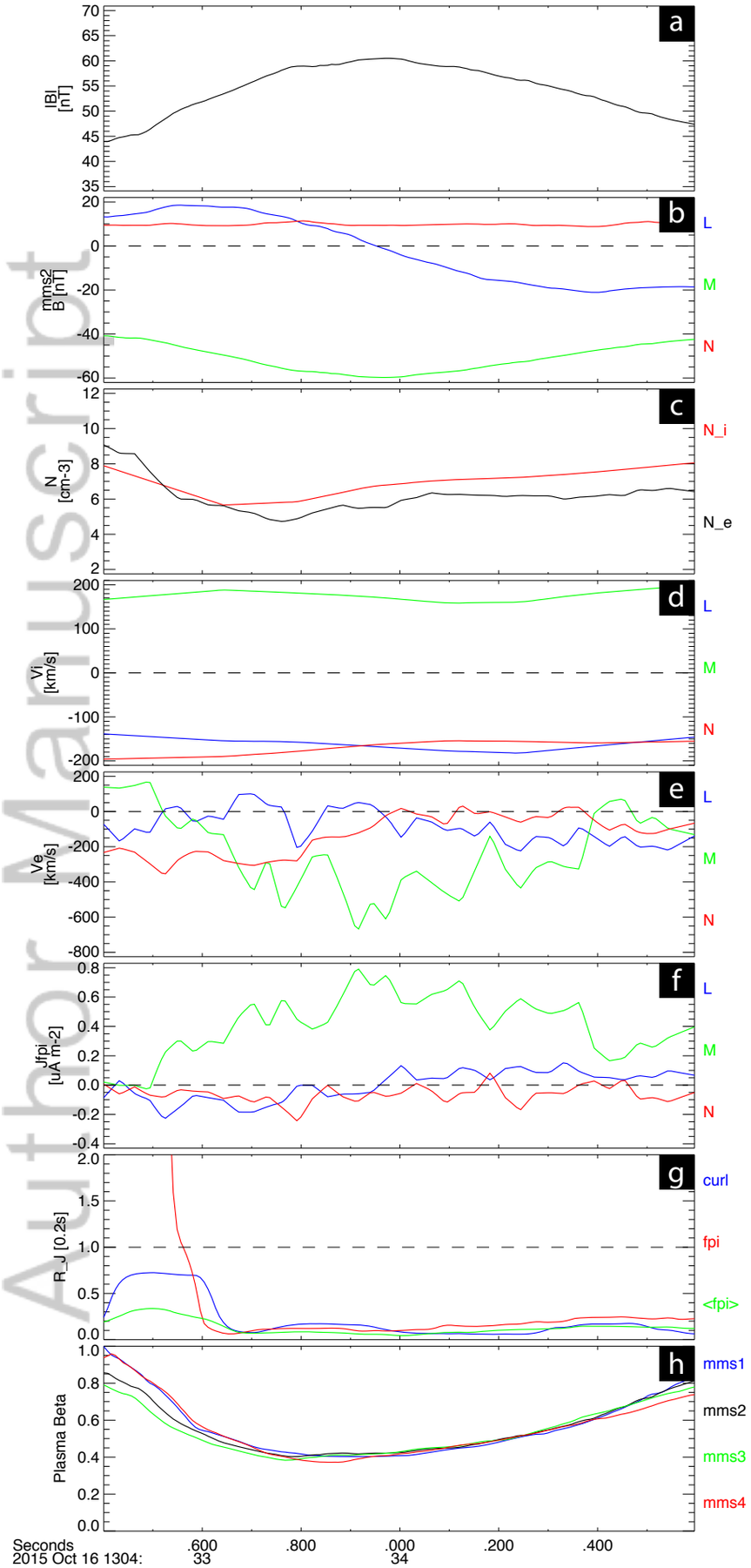

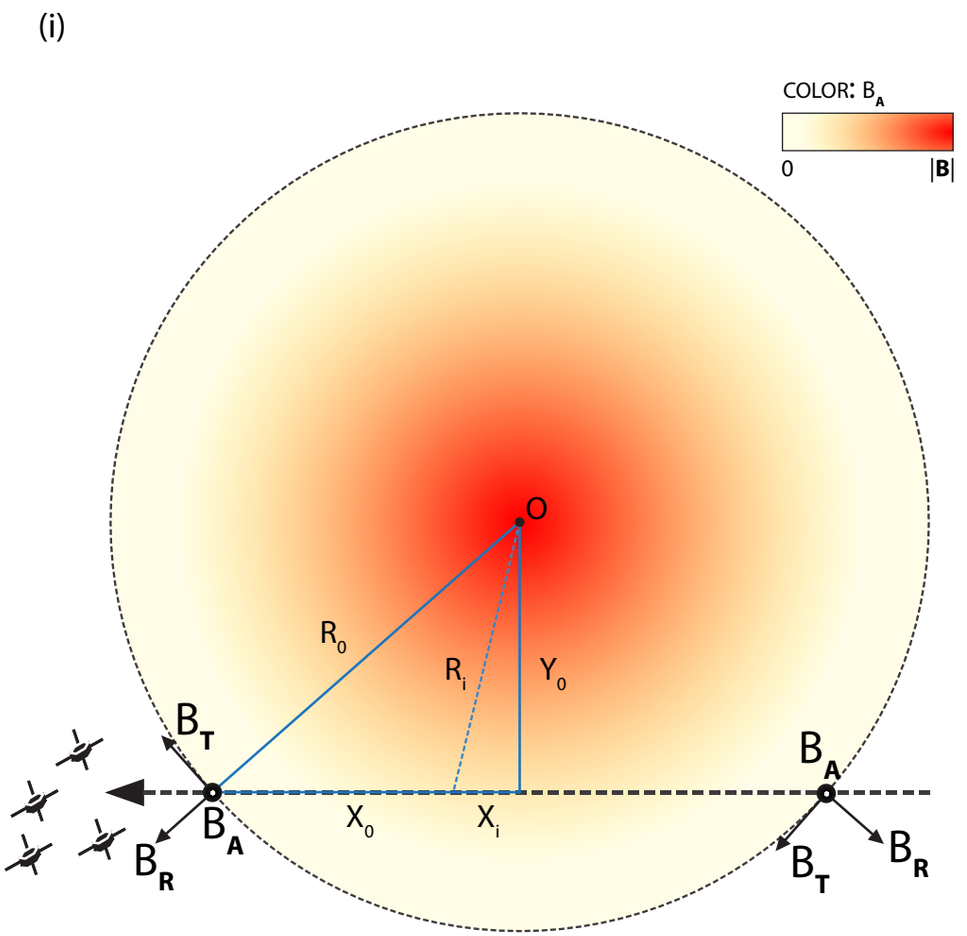

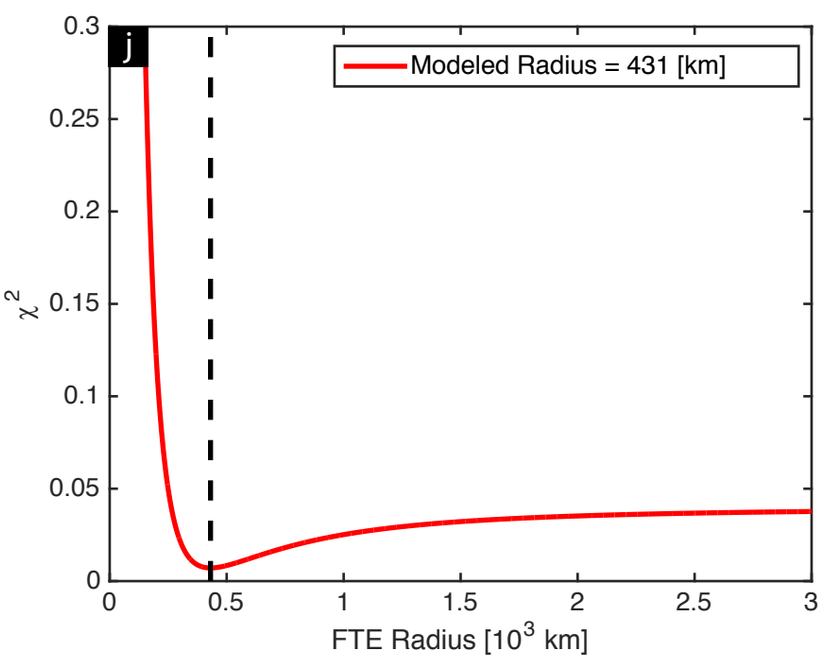

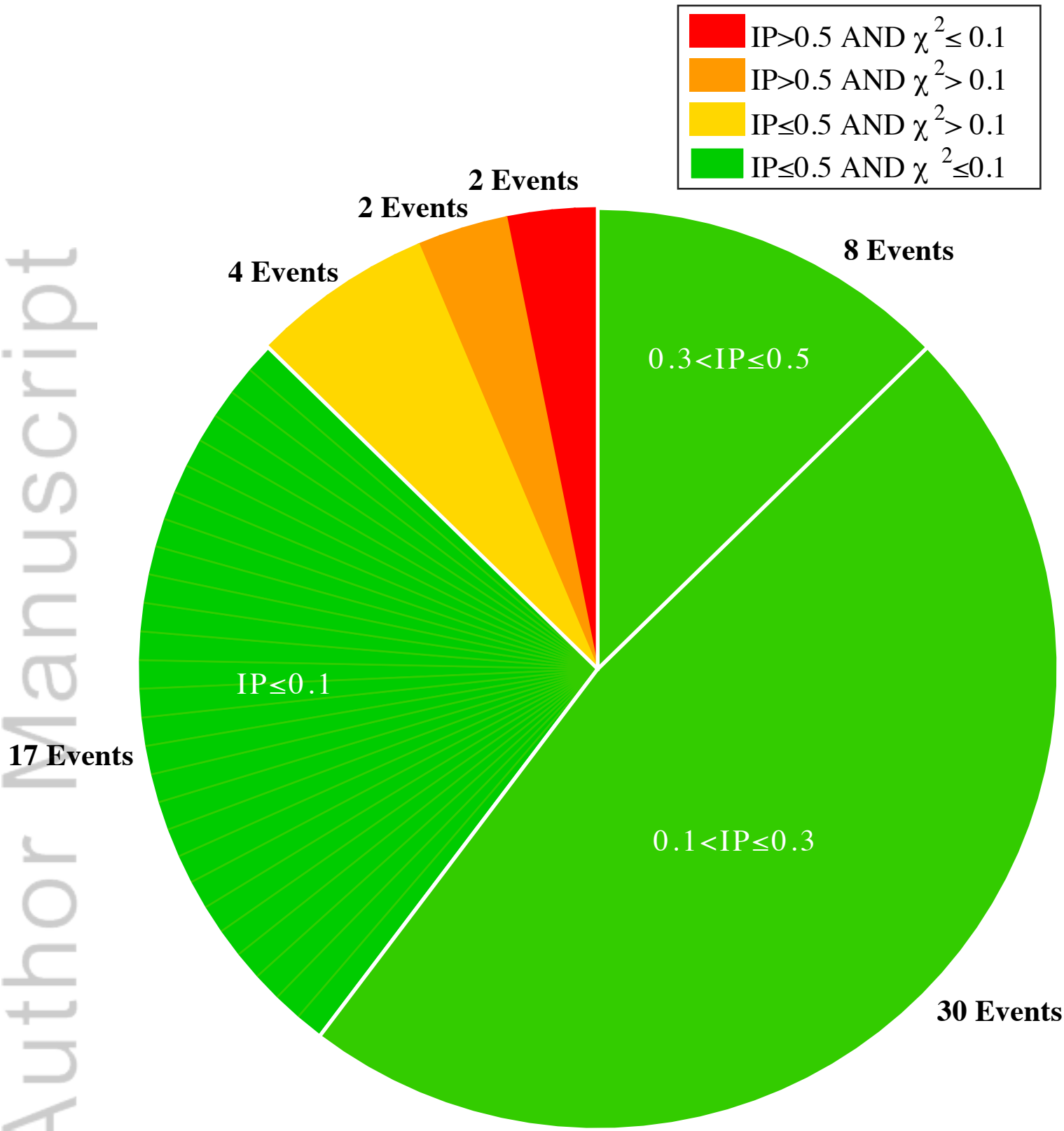

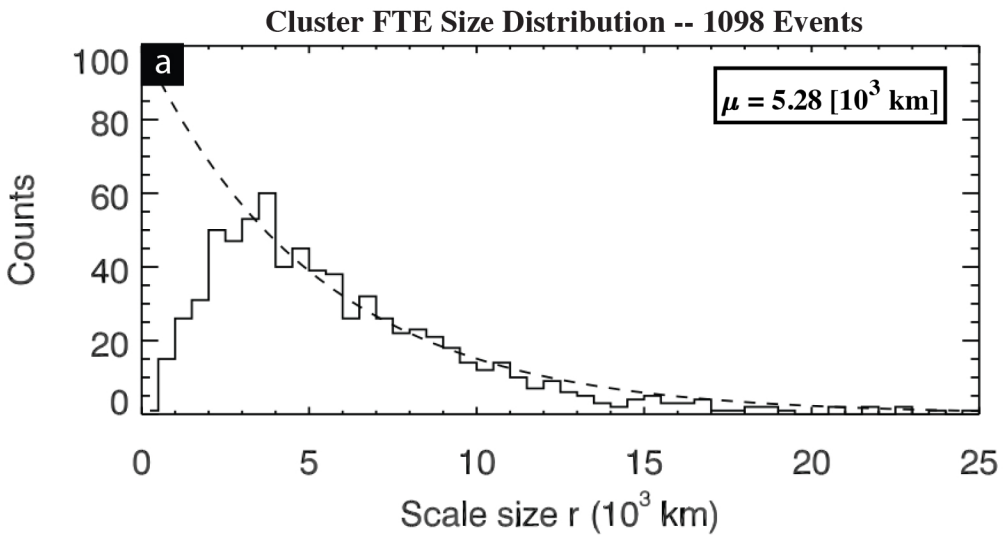

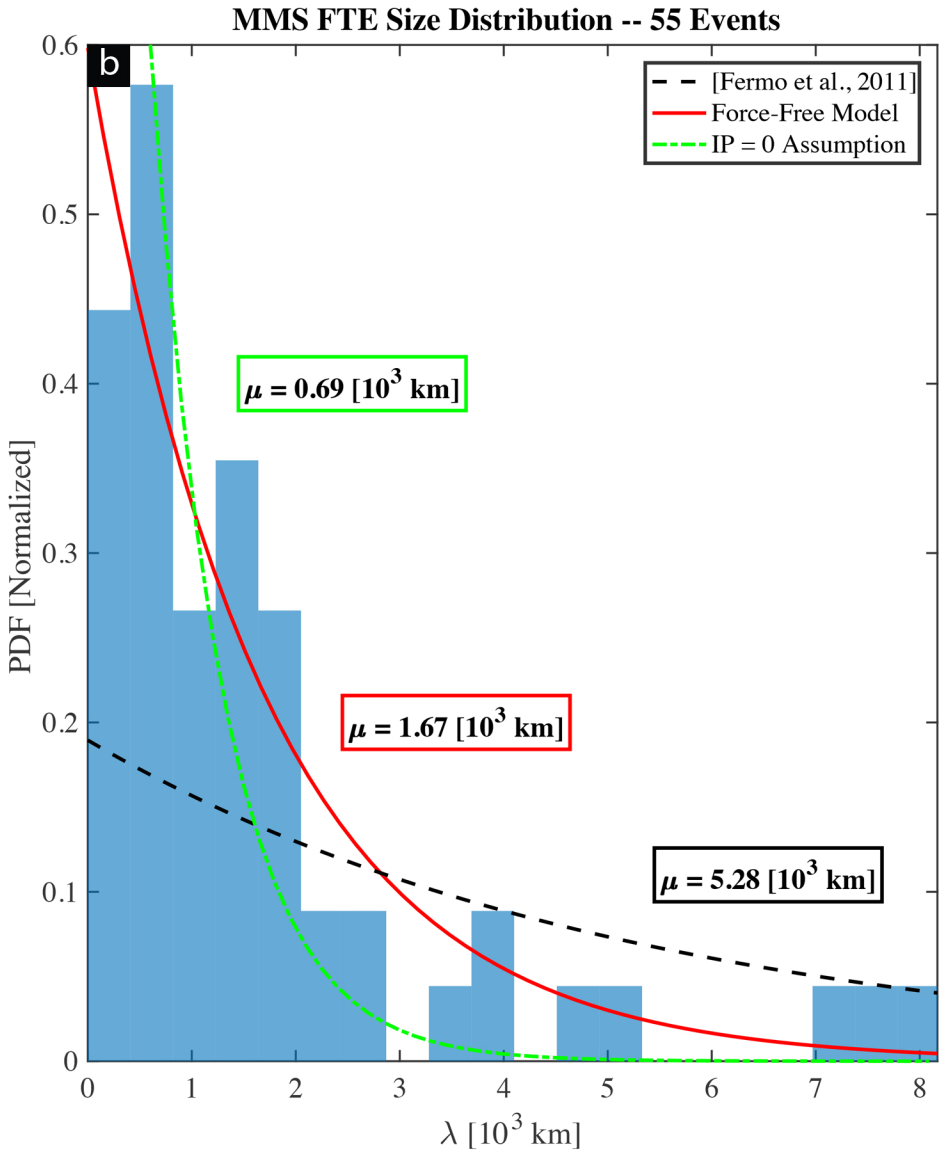

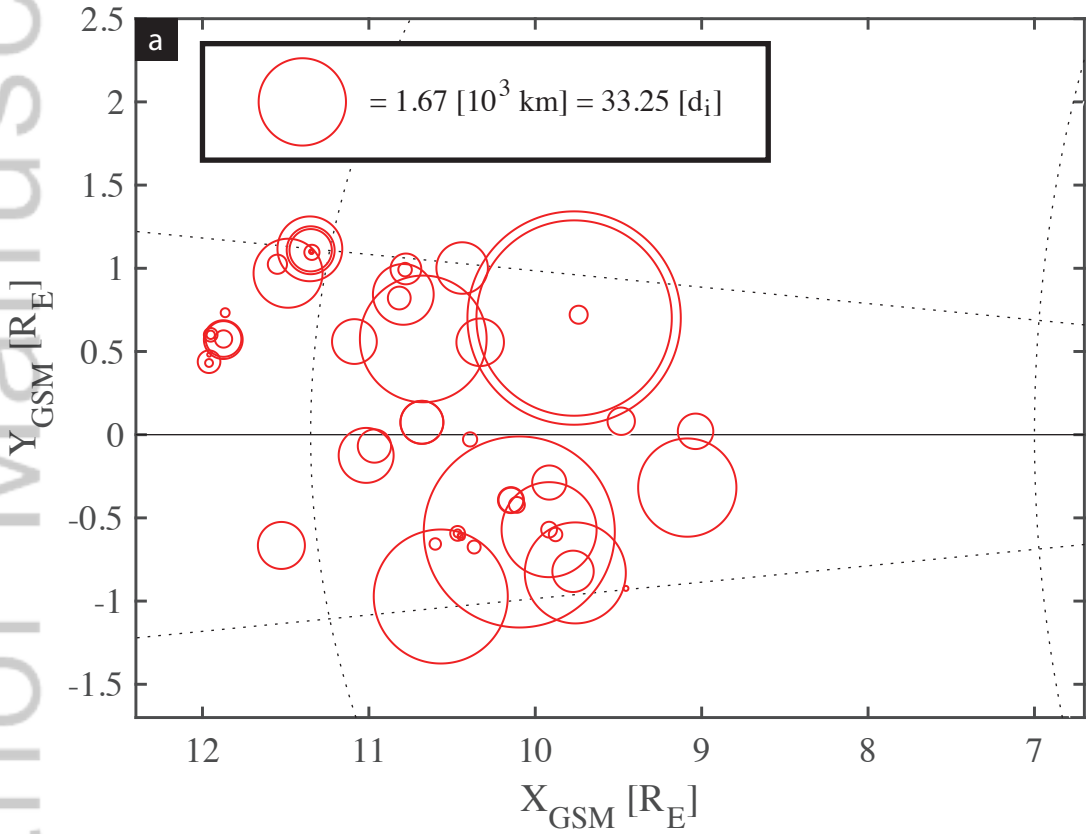

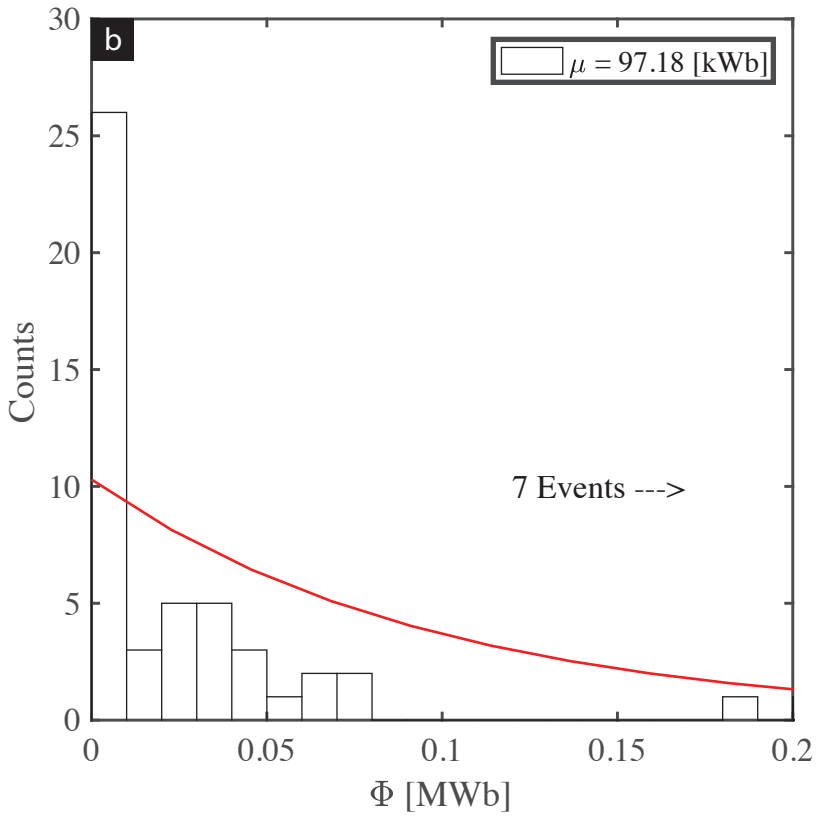

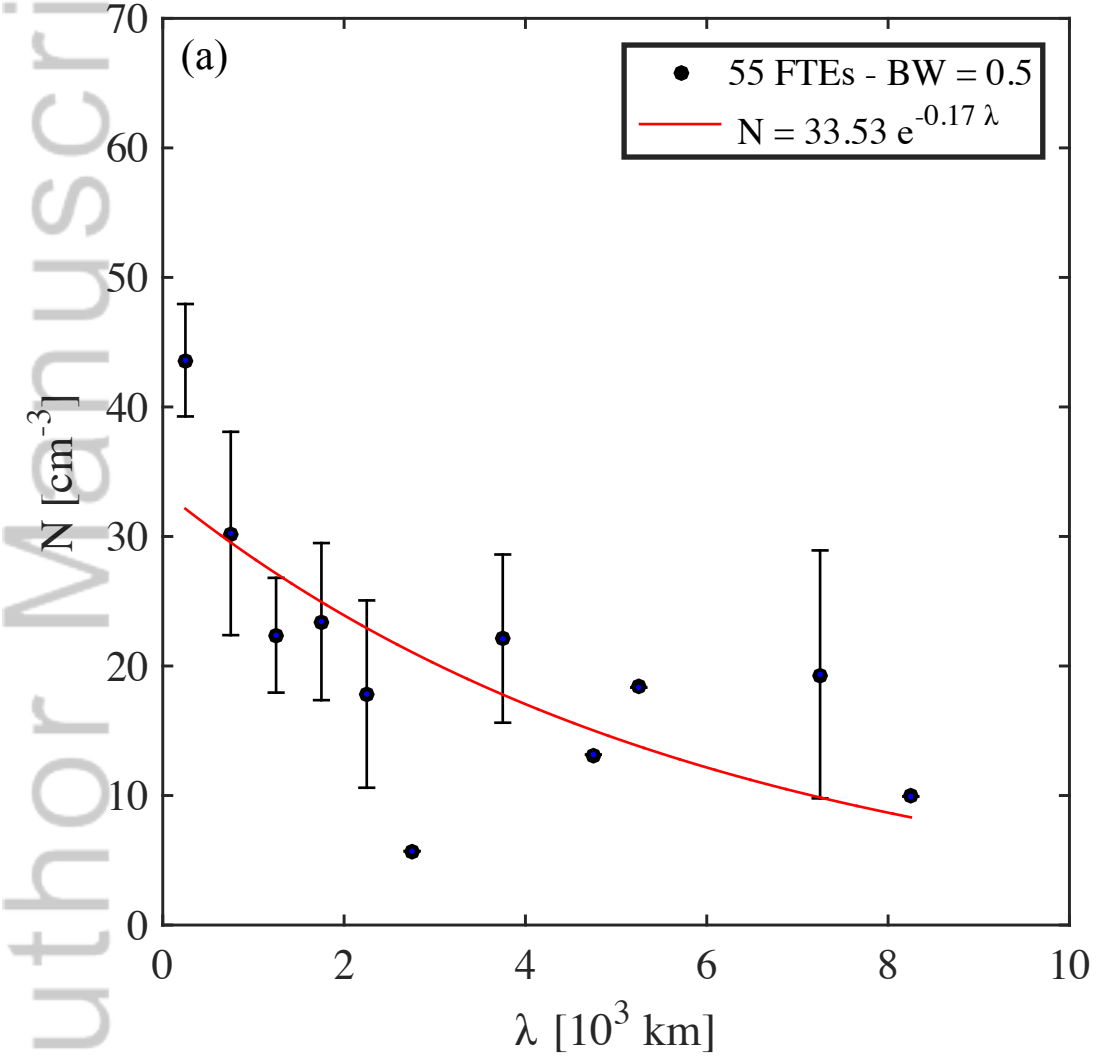

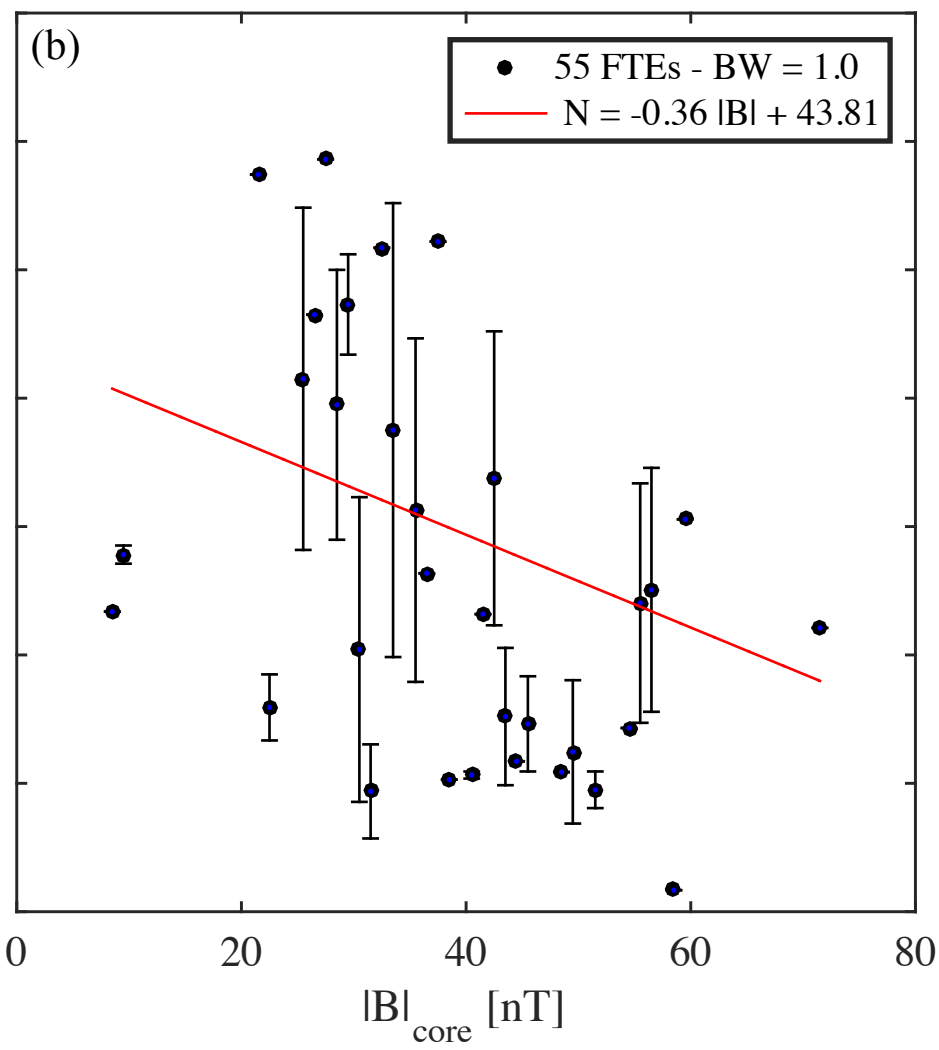

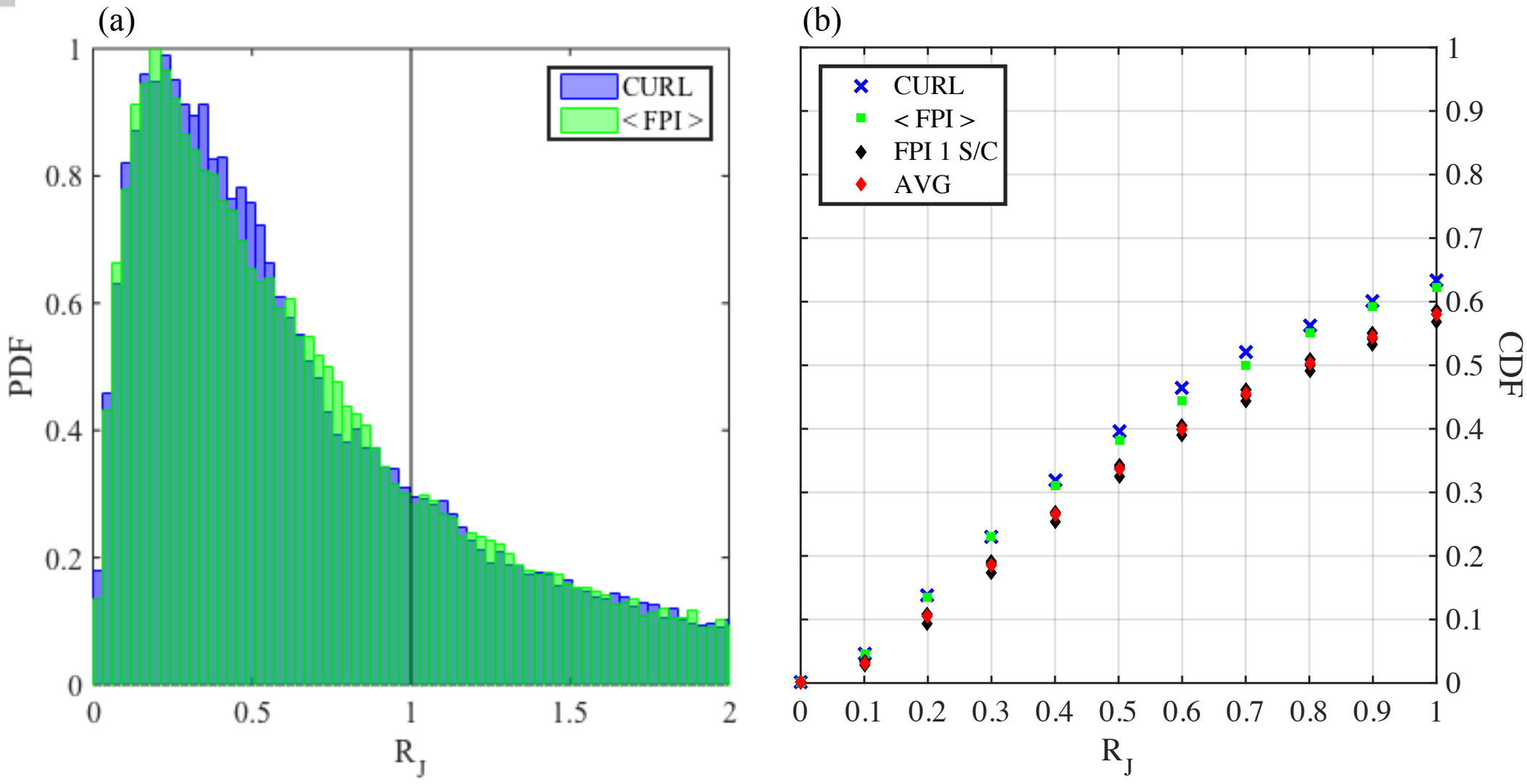

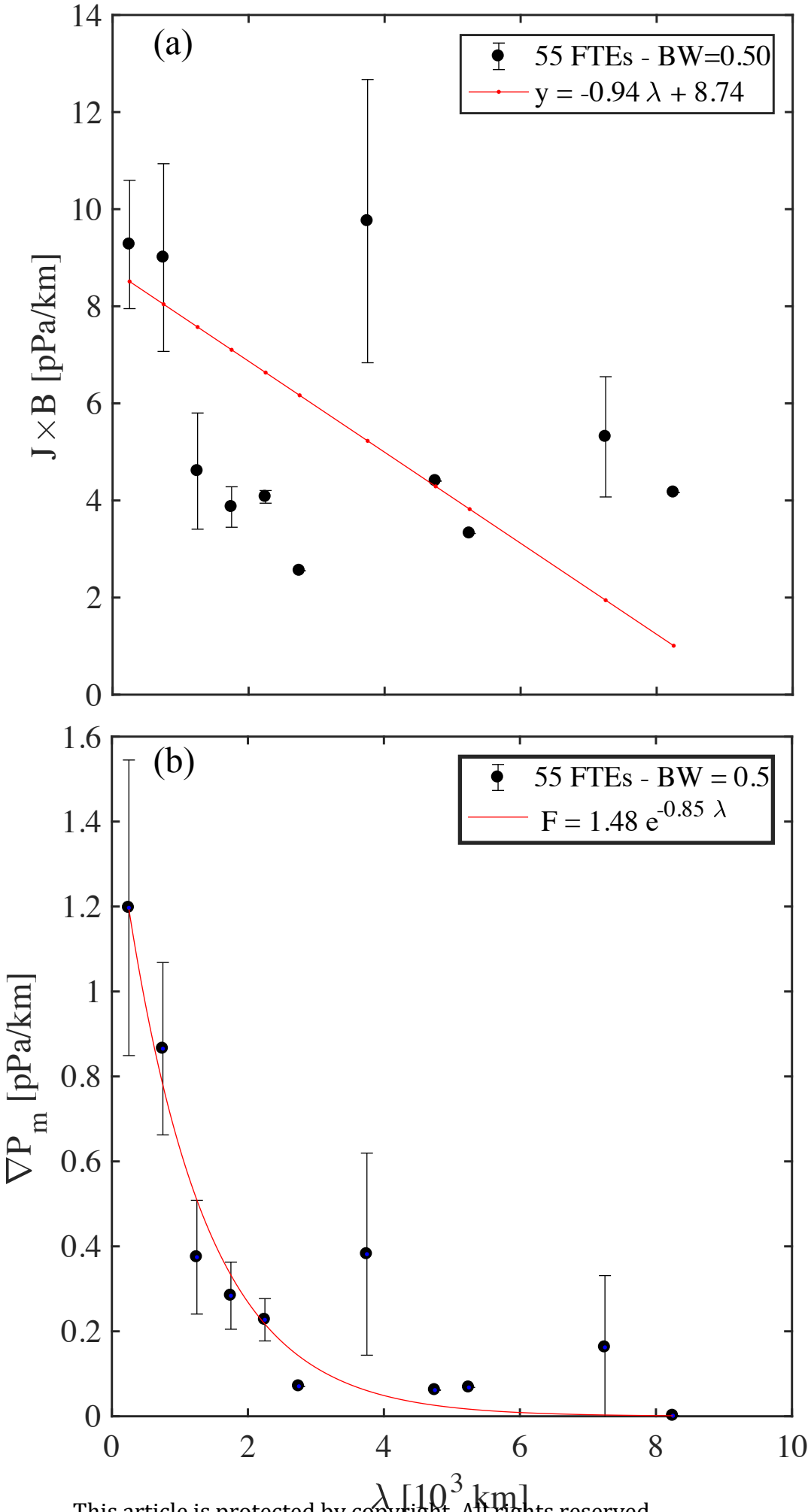

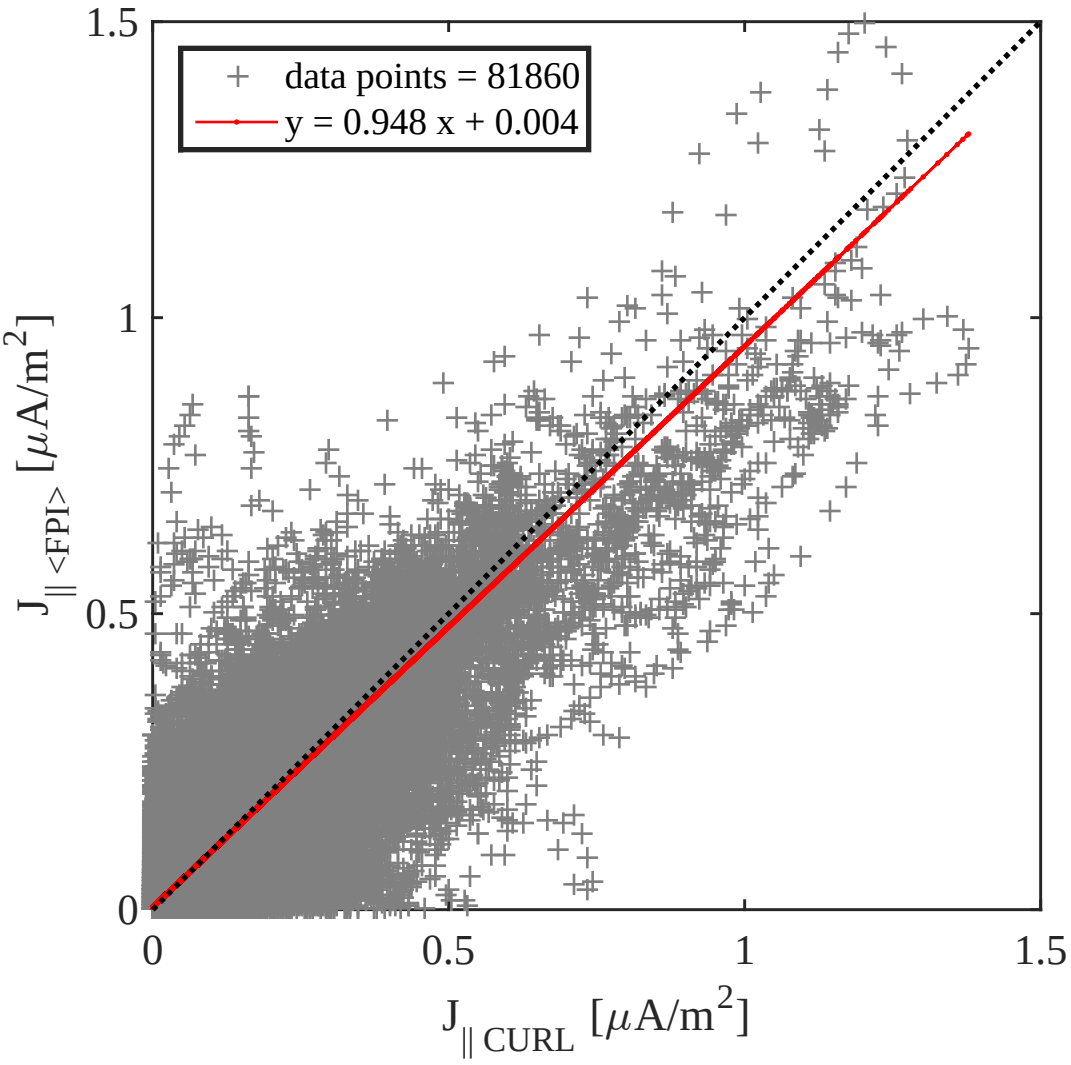

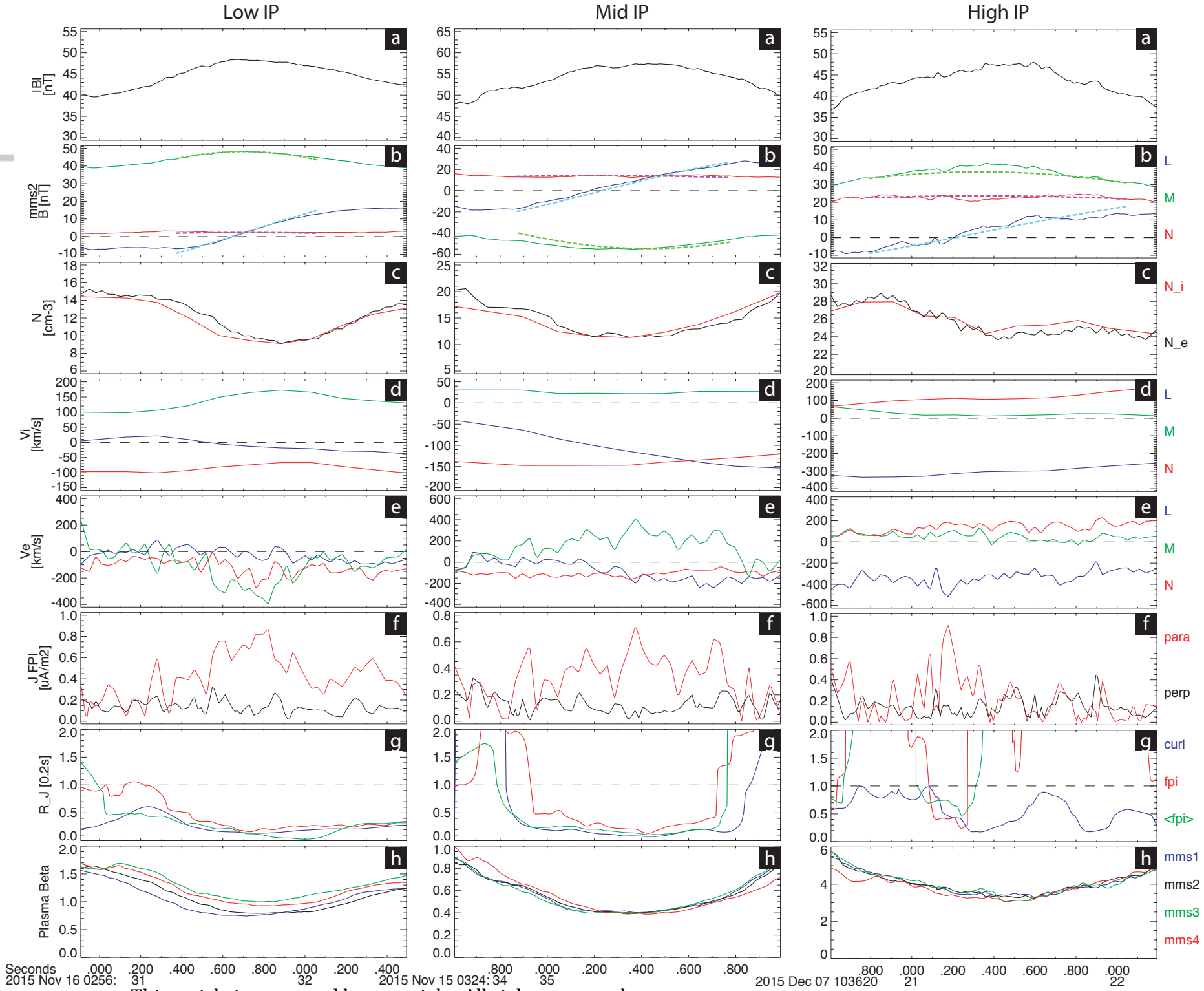

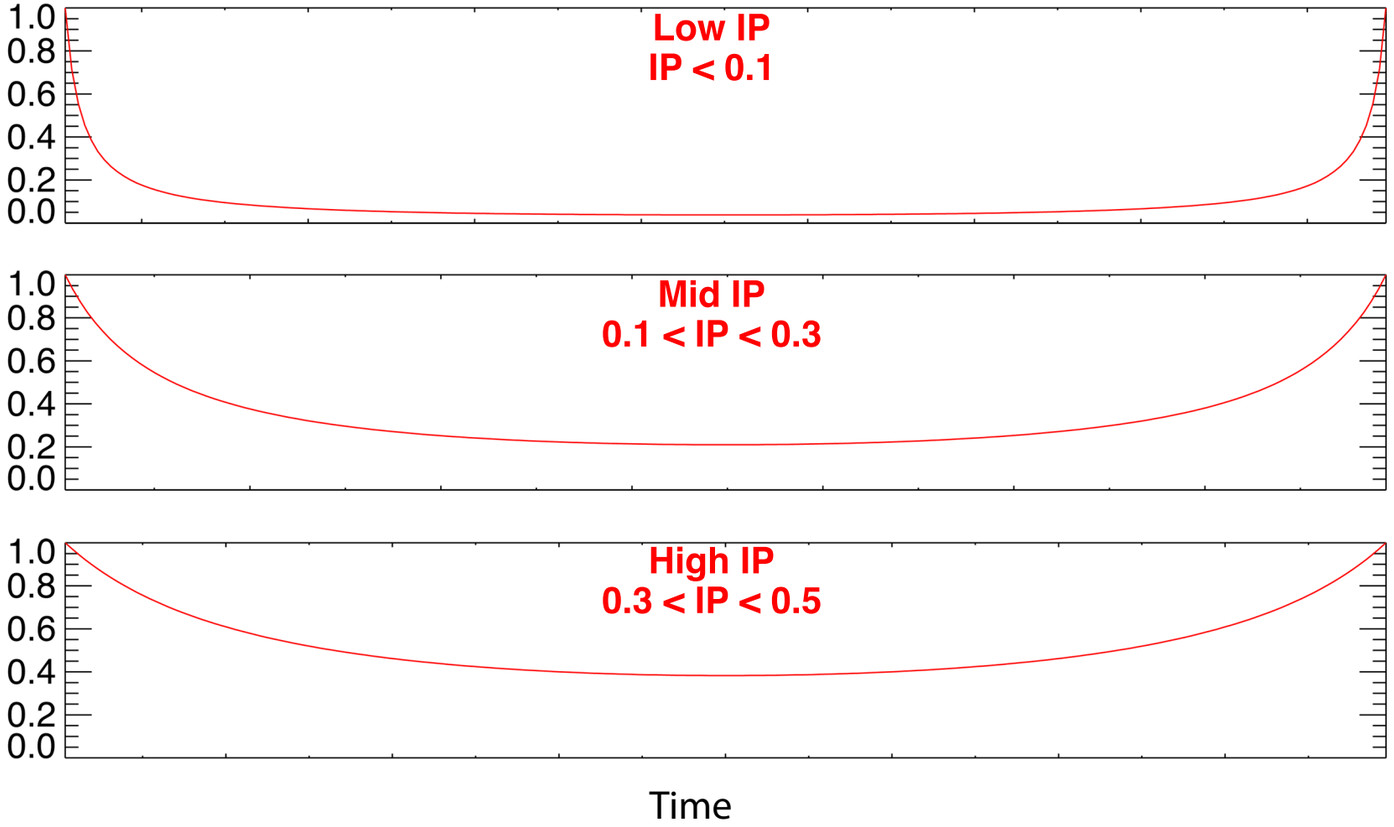

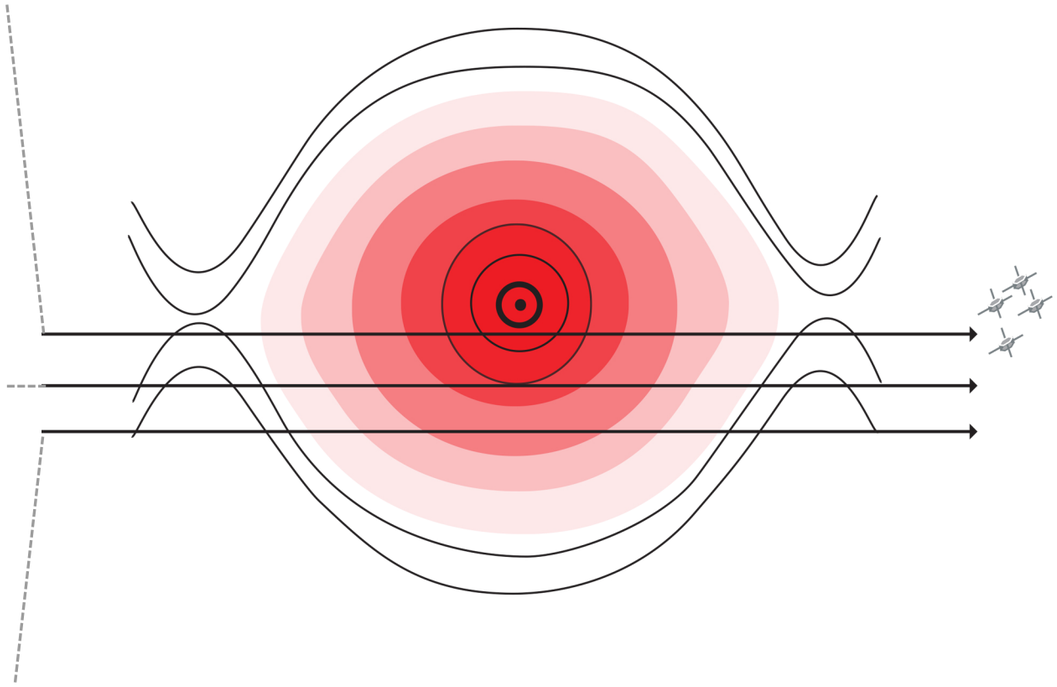

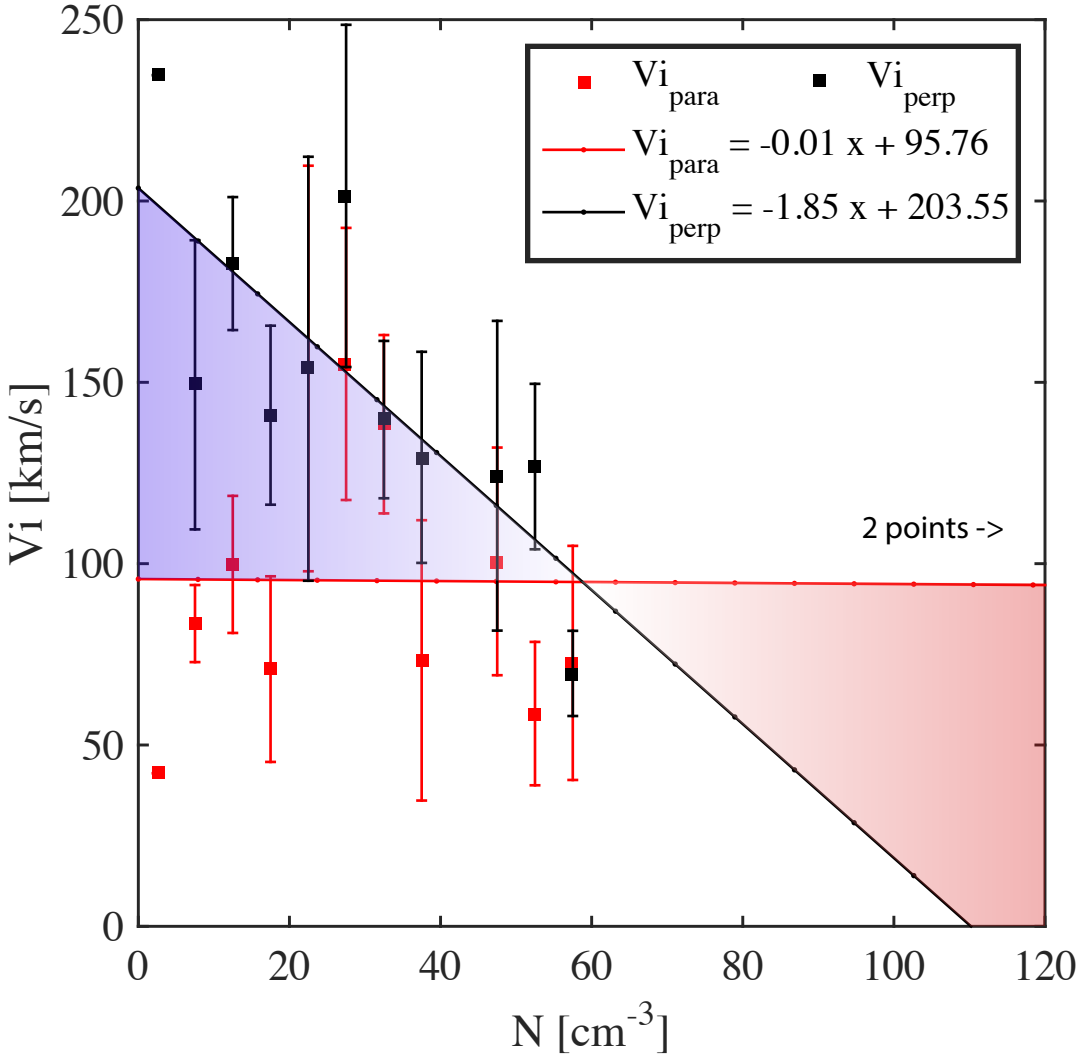

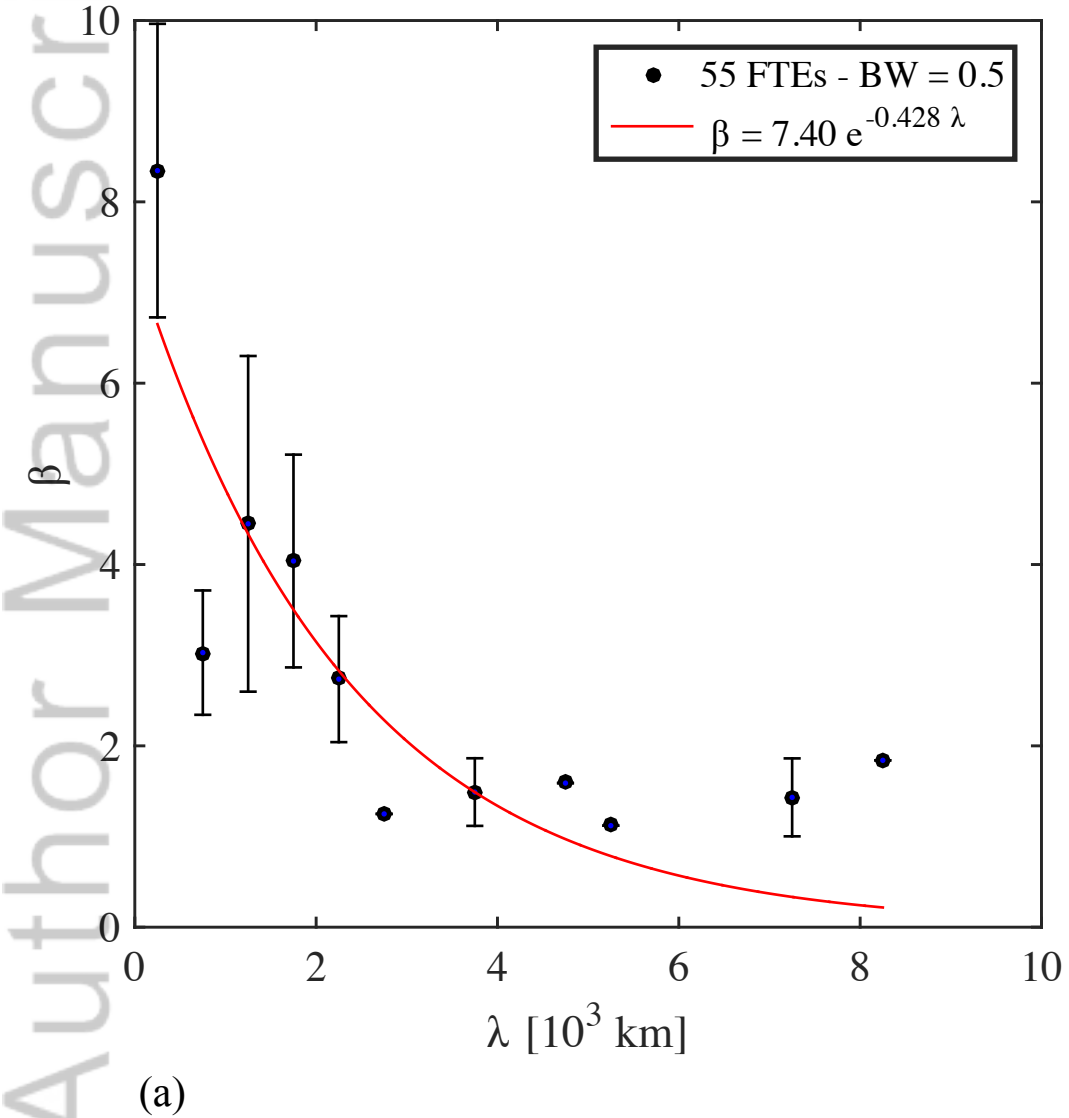

(a)

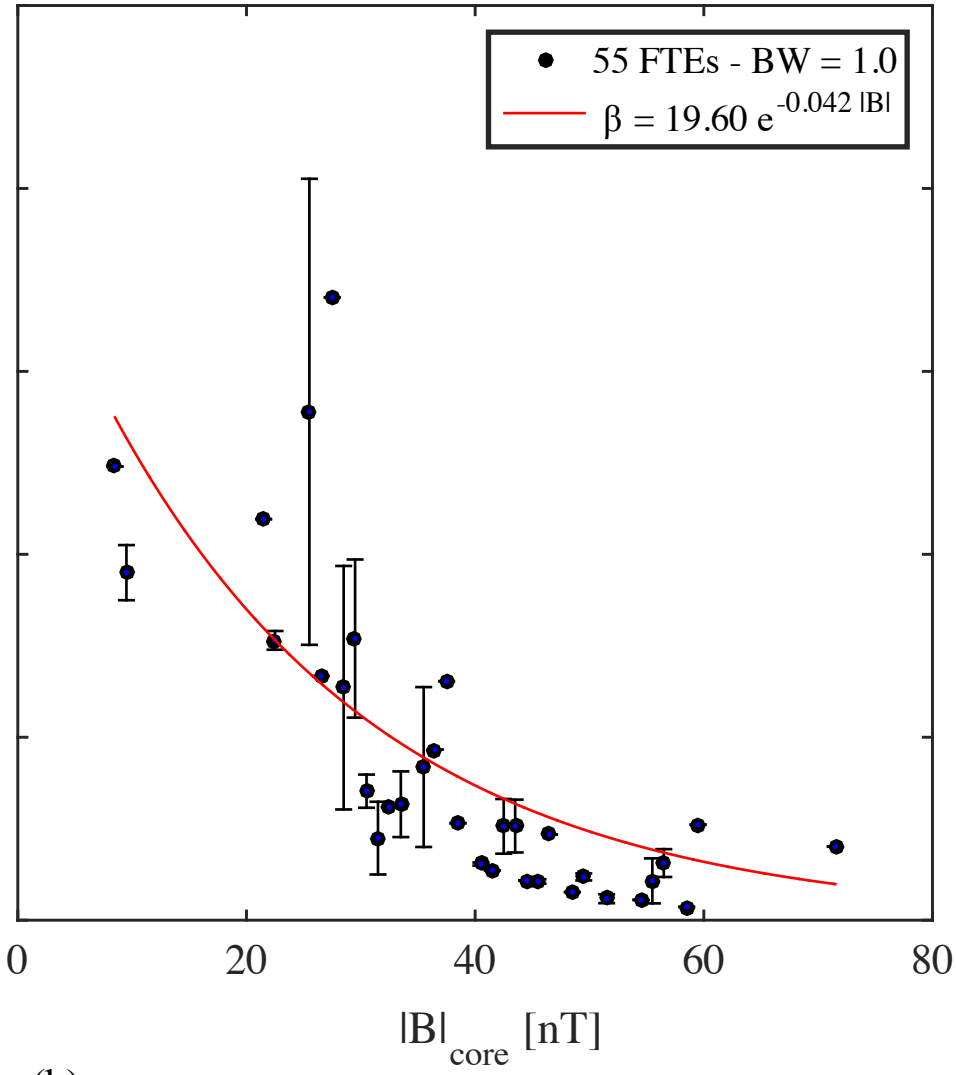

(b)

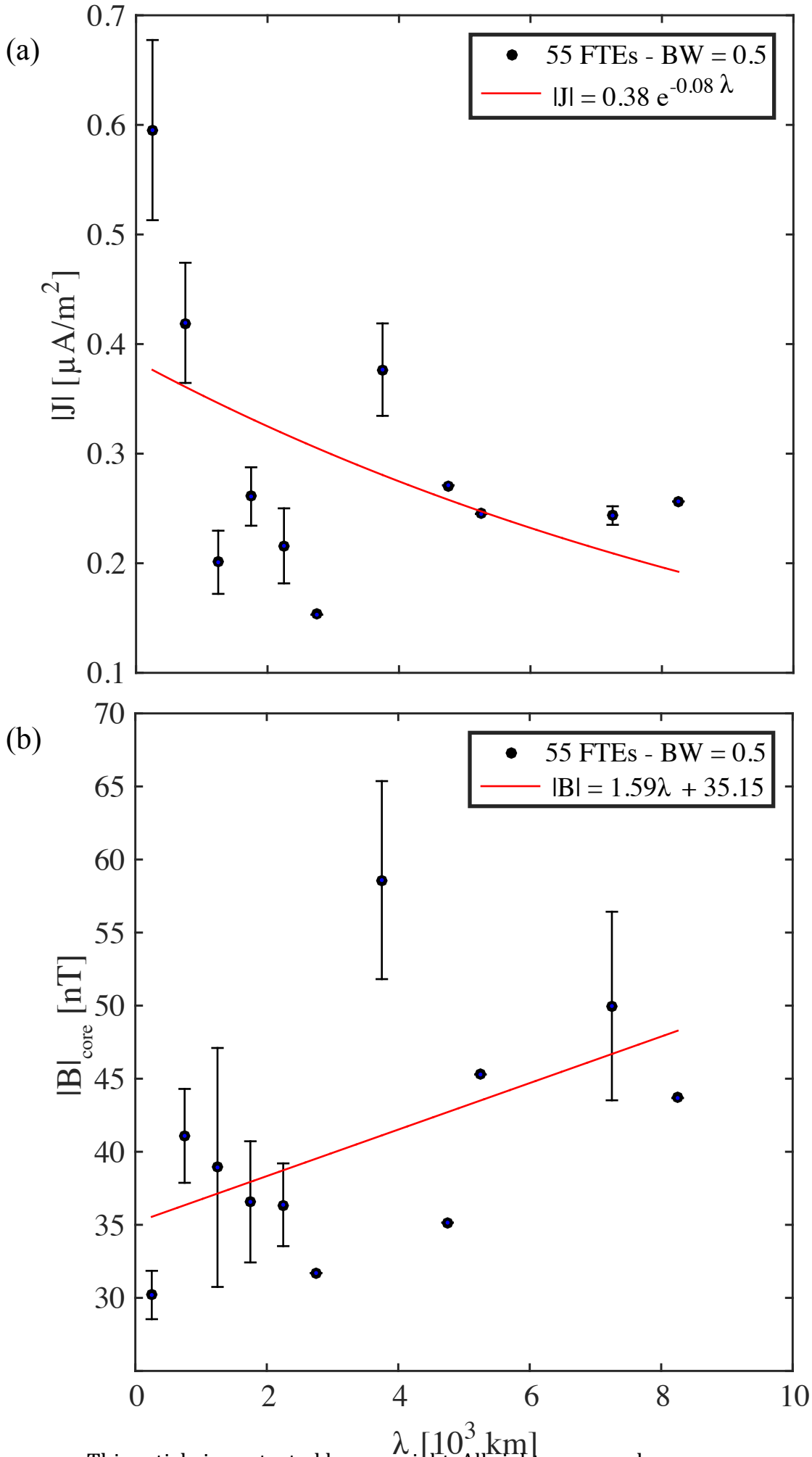

Table I. GSE to LMN coordinate transformation for three ion-scale FTE-type flux ropes.

Event #	λ_1	λ_2	λ_3	$\hat{\mathbf{L}}$ [GSE]	$\hat{\mathbf{M}}$ [GSE]	$\hat{\mathbf{N}}$ [GSE]
1	86.2	9.8	0.1	[0.723, -0.045, -0.690]	[-0.151, 0.963, -0.222]	[0.675, 0.264, -0.689]
2	270.4	20.2	0.6	[-0.997, -0.046, 0.065]	[0.061, -0.966, 0.250]	[0.051, 0.253, 0.966]
3	105.2	6.3	0.03	[-0.966, 0.135, 0.221]	[-0.086, -0.972, 0.218]	[0.244, 0.192, 0.951]